BOREAS An international journal of Quaternary research

A quasi-continuous long-term (5 Ma) Mid-European mountain permafrost record based on fluvial magnetic susceptibility and its contribution to the explanation of Plio–Pleistocene glaciations

ZOLTÁN PÜSPÖKI, GÁBOR MARKOS, TAMÁS FANCSIK, LÁSZLÓ BERECZKI, LÁSZLÓ FERENC KISS, EDIT THAMÓ-BOZSÓ, ZITA KRASSAY, PÉTER KOVÁCS, RICHARD W. MCINTOSH, ZOLTÁN VÁRI, FERENC STERCEL, ZOLTÁN LANTOS, VERA MAIGUT, KATALIN SÁRI, MIKLÓS RÁSONYI AND PHILIP L. GIBBARD

BOREAS

Püspöki, Z., Markos, G., Fancsik, T., Bereczki, L., Kiss, L. F., Thamó-Bozsó, E., Krassay, Z., Kovács, P., McIntosh, R. W., Vári, Z., Stercel, F., Lantos, Z., Maigut, V., Sári, K., Rásonyi, M. & Gibbard, P. L. 2025 (January): A quasi-continuous long-term (5 Ma) Mid-European mountain permafrost record based on fluvial magnetic susceptibility and its contribution to the explanation of Plio–Pleistocene glaciations. *Boreas*, Vol. 54, pp. 156–177. https://doi.org/10.1111/bor.12678. ISSN 0300-9483.

The low field magnetic susceptibility (χ_{LF}) measured in the 1116-m-long Dévaványa core (Pannonian Basin) is a quasi-continuous record of the Plio–Pleistocene Mid-European mountain permafrost development. The continuity of fluvial conditions is confirmed by seismic data, and the detrital origin of magnetite is indicated by frequency-dependent susceptibility measurements, scanning electron microscope, and hysteresis investigations. The χ_{LF} record is correlated to the $\delta^{18}O$ curve (LR04) supported by palaeomagnetic data. The colour of samples documents precession and obliquity cycles in local facies variations, but the χ_{LF} indicates the dominance of 100-ka eccentricity cycles in the linked mountainous permafrost events. Comparison with orbital solutions revealed that the long-term development of permafrost occurs as a result of amplitude modulation of the 100-ka eccentricity cycles. Increases in amplitude of the 100-ka cycles inhibits permafrost development due to shortened winters. Thus, if extremes are present, the permafrost regions are limited or disappear, but if the 100-ka eccentricity cycles are attenuated, permanent frost can extend into the temperate zone. This amplitude modulation may also be responsible for the early glaciations during the Pliocene, for the intensification of Northern Hemisphere glaciation, foreshadows cooling in the forthcoming 405-ka term, and allows the change from 41-ka cycles to 100-ka ones in the Mid-Pleistocene Transition to be explained. The 41-ka cycles are the result of obliquity-controlled changes close to the polar cycles, while 100-ka cycles occur when the amplitude attenuation of the 100-ka eccentricity cycles enables extended glaciations that suppress the regular 41-ka cycles. Higher mountains in the catchments enable higher resolution of permafrost records documenting even smaller glaciations. However, the similarities in the overall trends in χ_{LF} records of catchment areas with 1500-m difference in their altitude is a potential counter-argument when considering the role of tectonic elevations in the expansions of mountainous permafrost.

Zoltán Püspöki, Gábor Markos, Tamás Fancsik, László Bereczki, Zoltán Vári, Zoltán Lantos and Katalin Sári, Supervisory Authority for Regulatory Affairs, Alkotás út 50, Budapest H-1123, Hungary; László Ferenc Kiss and Péter Kovács, HUN-REN Wigner Research Centre for Physics, Konkoly-Thege Miklós u. 29-33, Budapest H1121, Hungary; Edit Thamó-Bozsó, Németh László u. 2/C, Dunakeszi H-2120, Hungary; Zita Krassay, Petőfi Lutheran Grammar School of Aszód, Régész u. 34, Aszód H-2170, Hungary; Richard W. McIntosh, Department of Mineralogy and Geology, University of Debrecen, Egyetem tér 1, Debrecen H-4032, Hungary; Ferenc Stercel, István út 21. IV/36, Debrecen H-4031, Hungary; Vera Maigut, Western Balkans Green Center, Naphegy tér 8, Budapest H-1016, Hungary; Miklós Rásonyi, HUN-REN Alfréd Rényi Institute of Mathematics, Reáltanoda utca 13-15, Budapest H-1053, Hungary; Philip L. Gibbard (corresponding author: plg1@cam.ac.uk), Scott Polar Research Institute, University of Cambridge, Lensfield Road, Cambridge CB2 1ER, UK; *received 7th June 2024, accepted 9th October 2024.*

Although the main sites of the Pliocene–Pleistocene glaciations are continental regimes, as a result of the strong denudation of evidence of antecedent glaciations, terrestrial records of cold events, and especially those dating from the Pliocene Epoch are rare and discontinuous (reviewed by De Schepper *et al.* 2014). This is the main reason why, whereas Milankovitch's theory was inspired by Mid-European mountainous glaciations (Milankovitch 1941), its accurate climatostratigraphical confirmation was established based on continuous marine records since the beginning (e.g. Hays *et al.* 1976; Imbrie & Imbrie 1979, 1980). This was enabled by the re-explanation of the $\delta^{18}O$ variations in the marine records as a proxy for changes in the global – but mostly terrestrial – ice volume (Shackleton 1967) that led to the extended set of marine palaeoclimate studies culminating in the global stack of marine records (Lisiecki & Raymo 2005).

Although this shift of focus from terrestrial to marine records was very fruitful, revealing a wide range of continuously recorded palaeoclimate proxies, it must be considered that the recorded marine changes, and especially the $\delta^{18}O$ variation, are not the causes but the consequences of terrestrial glaciations. These terrestrial glaciations, according to the Milankovitch theory, are controlled orbitally by changes in solar insolation. From this perspective, a direct and focused proxy of the changes in the terrestrial insolation, especially around

DOI 10.1111/bor.12678

the freezing-point of water, like a thermometer stuck into the soil and recording the frost on the surface over millions of years, may be as vital in palaeoclimate interpretations as the second equation in simultaneous equations of two unknowns.

Low field magnetic susceptibility (χ_{LF}) recorded in the Quaternary fluvial succession in the Pannonian Basin (Fig. 1B) has already been explained and used as a proxy for the mountain permafrost development in a fluvial catchment (Püspöki *et al*. 2016). It was revealed that this permafrost signal is not affected by the geological composition, but by the hypsometric features of the catchment (Püspöki *et al*. 2020, 2021b). The χ_{LF} records from the Pannonian Basin were correlated to the sea-floor isotope stratigraphy (Marine Isotope Stages – MIS), thus the Quaternary permafrost development of the Alpine and Carpathian region was reconstructed in general (Püspöki *et al*. 2021a) and in different settings (Püspöki *et al*. 2023).

Following on from these conclusions, the present authors attempted to extend their investigations through the Pliocene–Quaternary boundary, down to the base of the Pliocene, to test if the intensification of Northern Hemisphere Glaciation (INHG) and the early but moderate cold events of the Pliocene Epoch can be detected in a fluvial χ_{LF} record. The investigated section was the Dévaványa borehole, because this is the most complete palaeomagnetically documented long core in the region. To ensure a direct comparison with the already published Quaternary Pannonian fluvial sections, besides the regular χ_{LF} measurements, all the complementary magnetic investigations presented in the fluvial studies referred to above were performed on the Pliocene section of the long core. In this paper, we present the results and discuss some possible consequences for the Pliocene–Quaternary climate models.

Geological background

The concept of 'early postglacial fluvial magnetic episodes'

In their pioneering work Nádor *et al*. (2003) published fluvial χ_{LF} records of the quasi-continuous Quaternary fluvial succession of the Dévaványa and Vésztő boreholes. They recognized Milankovitch-scale cycles, but interpreting the χ_{LF} variations as a result of grain-size variations, their explanation was restricted to climate-controlled fluvial facies variations.

The investigation was extended involving all the long cores of the Körös Basin (Püspöki *et al*. 2016). It was revealed that (i) the χ_{LF} variation is independent from grain-size variation, (ii) the responsible magnetic phase is the detrital magnetite of various grain sizes originating from the mountainous catchment, and (iii) based on a simultaneously measured clay mineralogical proxy, the χ_{LF} maxima occur before the maxima of weathering intensity.

Thus, 'early postglacial fluvial magnetic episodes' were concluded to be related to thawing of the permafrost in the mountainous catchment. The destabilization of mountain permafrost (Gruber & Haeberly 2009) produces huge amounts of rock fragments (Gruber & Haeberly 2007) and the released magnetic minerals of high χ_{LF} are transported to alluvial plains. However, with further warming, the advanced development of soils and vegetation causes a fast and general disappearance of magnetic minerals from the substrates of the catchment and thus from the fluvial load. This is because both magnetite (Fischer *et al*. 2007; Grimley & Arruda 2007; Chen *et al*. 2011) and ilmenite (Cornu *et al*. 1999; Schroeder *et al*. 2002) are rather unstable in soils of variable redox conditions.

This idea was challenged in another fluvial basin (Jászság Basin) of very different drainage and rock composition of the catchment (Püspöki *et al*. 2020). It was revealed that, assuming at least some sources of magnetite in the catchment areas, the climate-dependent χ_{LF} signal can occur and can be traced far into the basin in both fluvial channel and flood-plain environments. The subsequent inclusion of the Alps as a mountainous catchment in the investigation (Püspöki *et al*. 2021a) also confirmed the idea of 'early postglacial fluvial magnetic episodes' and revealed the importance of catchment orography, as the gradual retreat of the permafrost zone causes long-term temporal trends in the climatically controlled fluvial magnetic susceptibility episodes, causing upward decreasing trends in the χ_{LF} record.

The χ_{LF} records of 16 long cores have enabled basin-scale correlations and the correlation of 'early postglacial fluvial magnetic episodes' to the sea-floor stratigraphy (Lisiecki & Raymo 2005). However, in contrast to loess susceptibility for example, the fluvial early postglacial susceptibility maxima were correlated with the cold intervals of the marine isotope stages, since regardless of their temporal delay, they are clearly related to and determined by the preceding cold period, i.e. the spatial extension of the recorded permafrost event. As a result, the Quaternary development of mountain permafrost in the Alps (Cremonese *et al*. 2011) and Carpathians (Popescu *et al*. 2017) of global significance (Obu *et al*. 2019) was interpreted stratigraphically (Püspöki *et al*. 2021b).

Meanwhile, three long cores of a source-proximal fluvial mega-fan (Maros Fan) were investigated (Püspöki *et al*. 2023) and the concept of 'early postglacial fluvial magnetic episodes' was confirmed by two additional arguments: (i) extended frequency dependent susceptibility measurements, together with hysteresis and scanning electron microscope (SEM) investigations, confirmed that the χ_{LF} is directly determined by the amount of fresh detrital magnetite; and (ii) the apparent

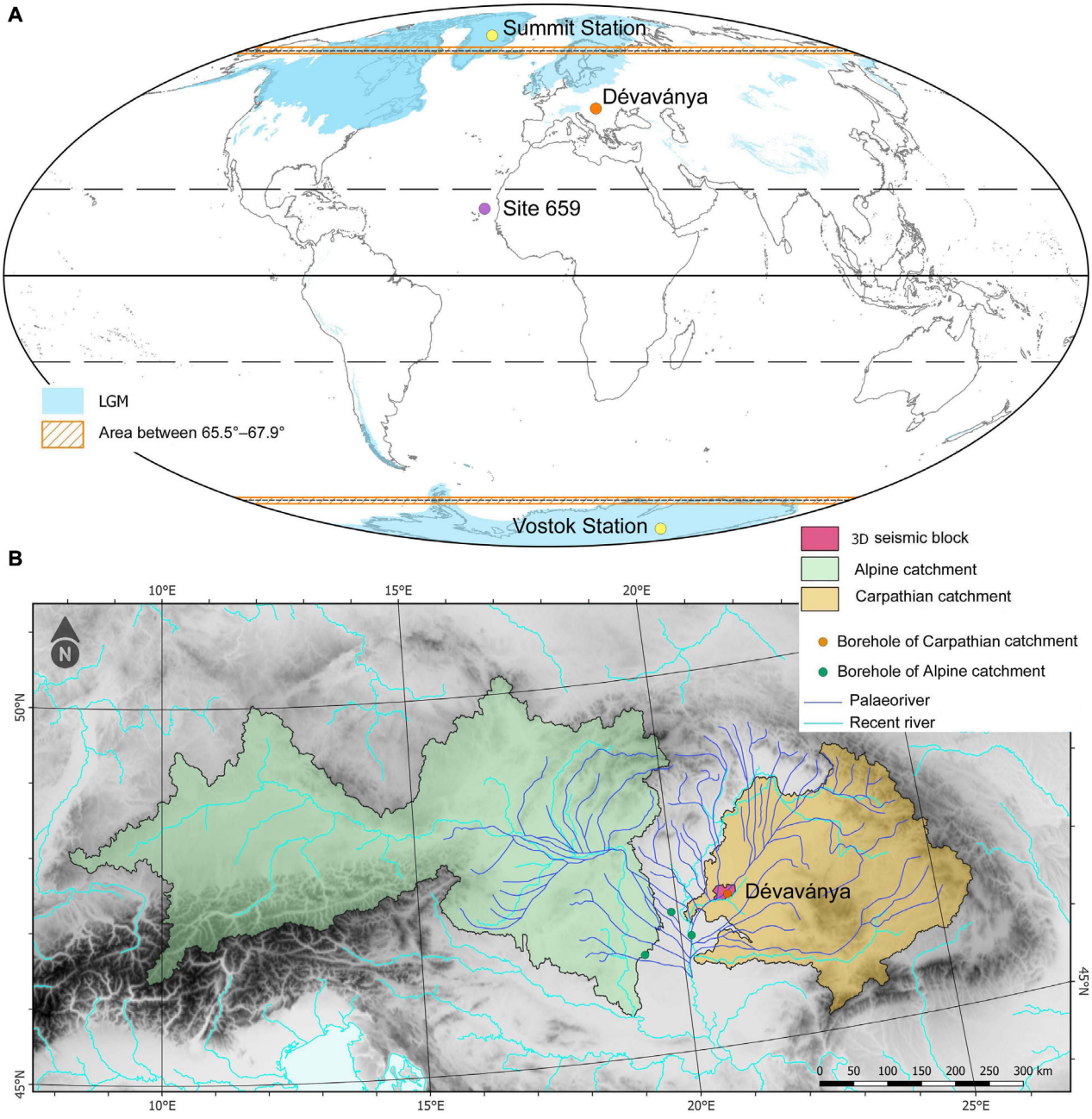

Fig. 1. Geographical location of the Dévaványa section, DSDP site, polar stations, and boreholes mentioned in the study. A. Global view during the Last Glacial Maximum (Ehlers *et al.* 2011). B. Related catchment areas of the Pannonian Basin with recent and Pleistocene drainage networks, and the extension of the 3D seismic block around the Dévaványa section. For the names of boreholes related to the Alpine catchment see Fig. 10.

gradual increase in χ_{LF} towards the basin margin unambiguously indicated that the source of this detrital magnetite was the mountainous hinterland.

Late Miocene–Pliocene basin development and geochronology

Due to its petroleum geological importance, the Late Miocene–Pliocene infilling of the Pannonian Basin is very well documented by seismic and downhole data (e.g. Royden & Horváth 1988; Pogácsás *et al.* 1994; Juhász *et al.* 2007; Sztanó *et al.* 2013; Csató *et al.* 2015). From the viewpoint of the investigations presented here, one of the most important features of this basin's development is that up to the earliest Pliocene most of the open lacustrine environments disappeared or were restricted to the southernmost part of the basin, with fluvial–alluvial conditions becoming predominant.

This facies change is clearly expressed in vertical seismic sections by the upward evolution of clinoform–

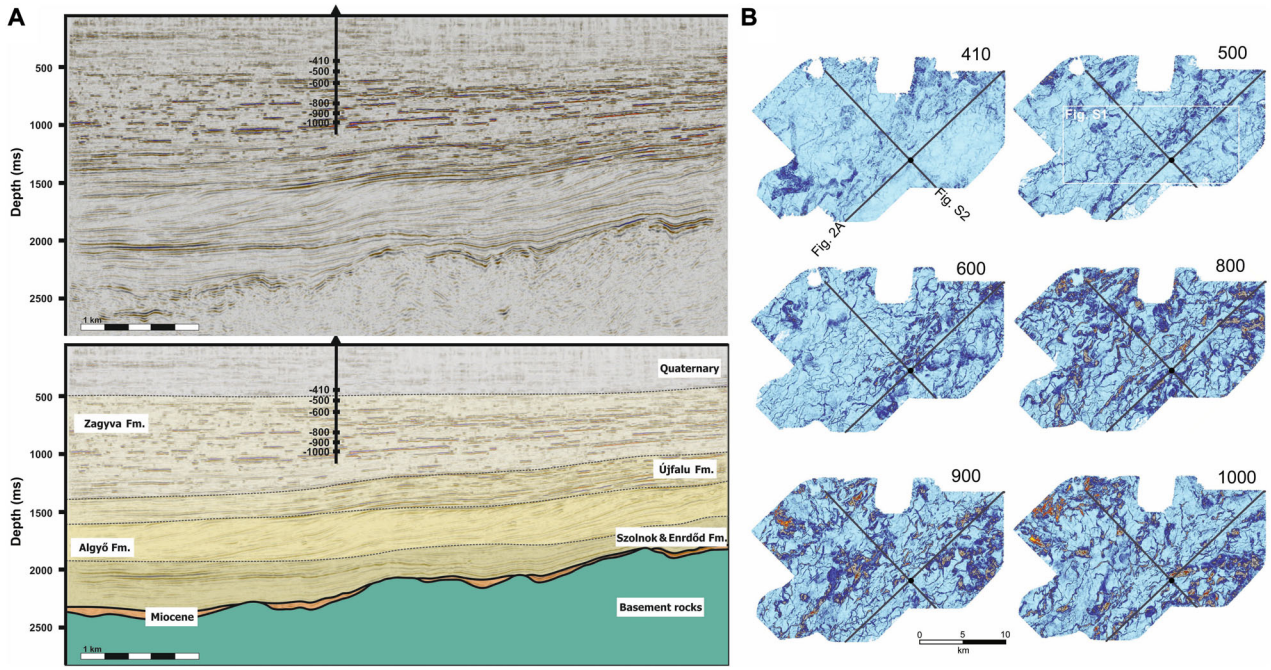

Fig. 2. Seismic data at and around the Dévaványa section. A. Dip-orientated vertical section (up) and its stratigraphical interpretation (down). The unit of vertical axis is in millisecundum (ms). B. Time slices at different depths (for the vertical position of maps see the Dévaványa borehole in panel A).

clinotheme structure to a dominantly horizontal–subhorizontal set of reflections (Magyar *et al.* 2013; Sztanó *et al.* 2013; Fig. 2A). In the regional lithostratigraphy the clinoform set of delta slopes is termed the Algyő Formation, whilst the subhorizontal set of reflections is referred to as the Újfalu and Zagyva formations. The nearshore setting of the Újfalu Formation frequently contains lignite-bearing lagoonal materials (Bükkábrány Member), but most of the alluvial terrains of the Zagyva Formation are characterized by meandering and/or anastomozing channels embedded in the overbank fines and the 'variegated clays' (Mahrez *et al.* 2023; Uhrin & Sztanó 2023). The alluvial facies conditions of the Zagyva Formation are expressed by seismic data based on frequent gaps along the reflections of large amplitude in vertical sections (Fig. 2A), and channel patterns revealed by time slices (Fig. 2B) of the 3D seismic sections.

The chronostratigraphical interpretation of this thick basin fill succession is not easy. The lack of foraminiferal and nanoplanktonic evidence results in the biostratigraphical scheme being mostly based on the endemic phytoplankton flora (Sütő-Szentai 2022) and on the advanced interpretation of evolutionary lineages of benthic molluscan fauna (Magyar 2015, 2021). Thus, the magnetostratigraphy has played a crucial role in the global correlation of this Late Miocene succession from the early studies (e.g. Cooke *et al.* 1979; Elston *et al.* 1994) right through to recent ones (e.g. Kelder *et al.* 2018).

Stratigraphy and lithology of the investigated borehole section

The Dévaványa borehole investigated here reaching 1116-m depth was drilled in the centre of the Körös Basin and represents the Zagyva Formation (Fig. 2A). It was one of the first long cores from which undisputed palaeomagnetic data where obtained proving the quasi-continuous Pliocene–Pleistocene sedimentation in the basin (Cooke *et al.* 1979). Both the substantial Quaternary palaeomagnetic epochs, i.e. the Brunhes and Matuyama chrons, together with the short-lived geomagnetic instability events (interpreted in Püspöki *et al.* 2021a) and those of the Pliocene, i.e. the Gauss and Gilbert chrons, were detected. However, the four small normal subchrons (Cochiti, Nunivak, Sidufjall, Therva) of the latter are represented by only two normal sections, so the borehole has been generally considered as just reaching the base of the Nunivak subchron. According to the palaeomagnetic data, the Quaternary base was encountered at 420 m, thus, from 420 to 1116 m the core represents the Pliocene succession.

Based on the downhole logs, and core descriptions, the observed lithology of the Dévaványa core is a monotonous alternation between sandy and silty strata the colour of which ranges from grey and greenish grey to yellow and reddish yellow (Fig. 3). Particularly in the lower, Pliocene part of the borehole a regular alternation between reddish and greyish beds is a characteristic feature. A dominantly fluvial molluscan fauna was found

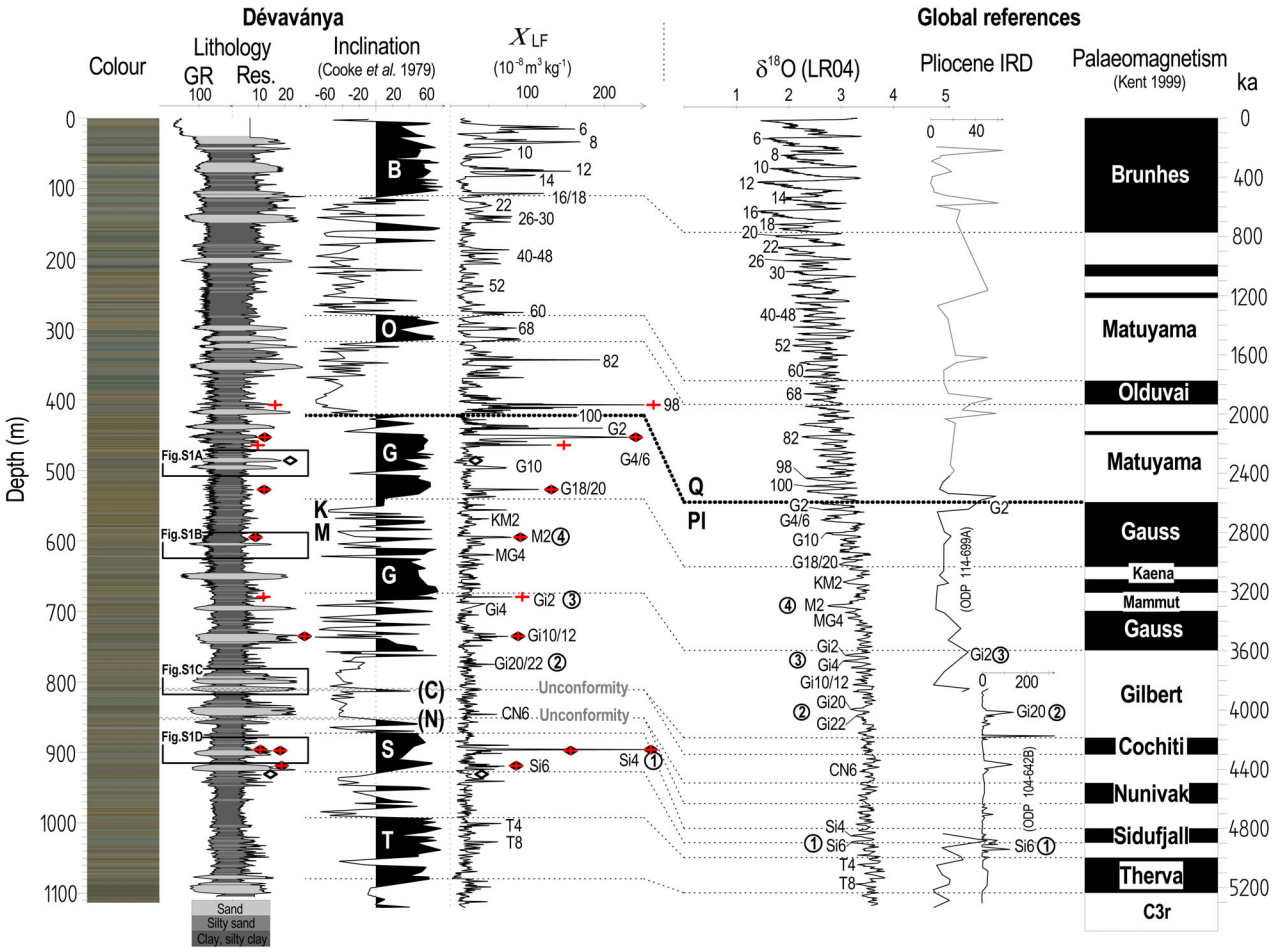

Fig. 3. Low field magnetic susceptibility (χ_{LF}) of the Dévaványa section, together with wireline log, lithology, palaeomagnetic data (Cooke *et al.* 1979) and measured colour, in correlation with marine isotope stages (LR04 – Lisiecki & Raymo 2005), ice-rafted detritus (IRD) records (ODP 114-699A is from Allen & Warnke 1991, ODP 104-642B is from Jansen *et al.* 2017) and palaeomagnetic epochs (Kent 1999). The red crosses indicate the position of samples investigated by SEM (Fig. 4), black squares indicate samples subjected to hysteresis investigations (Fig. 5), encircled numbers refer to the discussion in De Schepper *et al.* (2014), the frames in the lithology track refer to locations in Fig. S1.

in the upper 250 m of the borehole (Krolopp 1977). These shells were recently subjected to amino-acid investigations (Nelson *et al.* 2023). In the remaining part of the core there was no remarkable palaeontological material recovered, most probably reflecting the poor preservation potential of the succession.

Material and methods

The interpretation of the χ_{LF} as a fluvial facies feature requires that permanent fluvial facies are represented throughout the entire investigated section. To confirm the facies characteristics of the monotonous series of sand and silt layers, horizontal time slices of the enclosing 3D seismic block (Fig. 1B) were constructed at about 100-m (100-millisecundum) depth intervals. The time slices were visualized primarily by amplitude. The investigation was performed in Petrel® with RMS Amplitude seismic attribute. Root mean square (RMS) amplitude was used to display amplitude values in a specified window of stack data, as it provides a smoother amplitude estimate for multiple-amplitude attributes and is thus sensitive to changes in sediment grain size and to the occurrence of unconformities (Koson *et al.* 2014). However, since amplitude values are squared, the method is also sensitive to noise.

The magnetic susceptibility of the Pliocene section was recorded at ~0.5–1 m sampling intervals (~5 ka) depending on the observed lithology, using the inner parts of the cores. The number of samples in the Pliocene section is $n = 748$. The material was placed in plastic boxes $2.5 \times 2.5 \times 2.0$ cm. Measurements of χ_{LF} were made using an SI-2 susceptibility instrument operating at 750 Hz and at a peak field of 1 Oe at the laboratory of the Supervisory Authority of Regulatory Affairs (SARA). Frequency dependent susceptibility (χ_{FD}%) was measured on the selected set of samples ($\chi_{LF} >$

$\sim 60 \times 10^{-8}$ m^3 kg^{-1}) in a Bartington MS2 magnetometer at 470 and 4700 Hz.

To determine magnetic minerals, the magnetic fractions of representative samples were separated using a hand magnet (cf. Heider *et al.* 2001). The magnetic grains were studied using a Thermo Scientific Scios 2 dual-beam scanning electron microscope (SEM) with a Shottky cathode at 15 kV. An atomic number sensitive back-scattered electron detector was applied to show Fe-containing high contrast magnetic grains. The chemical compositions were measured using a BRUKER (SSD) energy dispersive spectrometer with ~70-s detection time with ~8000–10 000 cps. To perform quantitative evaluation of the magnetic minerals, hysteresis curves of selected samples were measured at room temperature ($T = 300$ K) in a SQUID magnetometer (Quantum Design MPMS-5S) in the magnetic-field range of $\pm H = 50$ kOe.

Bitmap images of the χ_{LF} samples in the $2.5 \times 2.5 \times 2.0$ cm transparent Plexiglass cubes, obtained using an image scanner, were used to quantify the colour of the samples. RGB components of the sediments were calculated by averaging the RGB values of 150×150 image pixels of each sample using code written in GNU Octave (cf. Nederbragt *et al.* 2005).

In the time series analysis, the re-scaling of the χ_{LF} record was performed by piece-wise linear interpolation, using AnalySeries (Paillard *et al.* 1996). The spectral estimations were made using the multi-taper method (MTM; Thomson 1982, 1990), which enables investigation of the statistical significance. The data were linearly detrended and pre-whitened; the number of tapers was six. Evaluating the statistical significance of spectral peaks, the spectral background was approximated with the quadratic fit of the log power vs. frequency data; the degrees of freedom were considered 12, i.e. twice the number of tapers (Weedon 2003). The fundamental Milankovitch frequencies, i.e. eccentricity, obliquity, and precession, for the last 5 Ma were used according to the analytical solutions (Laskar *et al.* 2004) and expressed spectrally also by MTM. The band pass filtering of χ_{LF} and orbital solutions together with the Hilbert transformations were performed by AnalySeries.

To reveal the temporal evolution of the re-scaled susceptibility records, a continuous wavelet transformation was also performed (Foufoula-Georgiou & Kumar 1994). In this procedure a Morlet mother wavelet was applied. Averaged wavelet power was extracted over the 84–119 ka band of the wavelet scale (cf. eq. 24 in Torrence & Compo 1998).

In the discussed geographical evaluations, the extension of the ice sheets was considered according to Ehlers *et al.* (2011). The GIS of the ice sheet, landmass, and latitudes was managed in the Mollweide projection, which is appropriate for world maps requiring accurate areas. The investigated catchment areas were designated based on Lehner and Grill (2013); the hypsometric curves were generated based on the ETOPO Global Relief Model.

Results

Log and 3D seismic facies interpretations

The coherence of log and seismic data enables reasonable facies interpretation of the investigated Plio–Pleistocene fluvial succession (Fig. S1) considering both architectural elements occurring in vertical profiles of logs (e.g. Miall 1996) and plan views of geomorphological components of the alluvial plain. The apparent sand bodies with large resistivity values and 5–10 m thickness in the logs are the prominent bar complexes of large rivers representing multiple sedimentation systems (Lewin & Ashworth 2014) with accessory and tributary channels of meandering, straight or low sinuosity (Fig. S1). Immediately above the bar complexes, silty sand of the channel proximal flood-plain can occur in logs (Fig. S1B–D) representing levee, crevasse splay, oxbow lake or pond, depending on its position and shape in 3D seismic images (Fig. S1A–C). These channel proximal facies, due to the diffuse or laminated occurrence of sand in the silt and silty clay, frequently occur with transitional colour in the 3D seismic slices attached mostly right next to the main channels.

The silty clay deposits of the distal flood-plain are represented by light blue colour on the seismic images and by low resistivity values in logs. However, thin but apparent meandering or strait channels of dark blue colour can be seen in seismic images in the distal flood-plain, indicating that the small tributary or accessory channels are also dominantly infilled by sand, causing significant seismic contrast. In the logs these secondary channels occur as apparent but thin (2 m) sand intercalations in the flood-plain silt, of lower resistivity relative to the main channels, indicating fine sand filling these flood-plain channels. Sometimes small headward-extending internal drainages can also be identified in distal flood-plains (e.g. Fig. S1A).

Considering the overall seismic patterns of the time slices (Figs 2B, S1), the dominant flow direction is NE to SW, with one or two main and a series of secondary channels. A progressive upward change in the drainage network can be observed as indicated by the decreasing drainage density, i.e. the ratio between channel and distal flood-plain conditions. This is again supported by the wireline log (Fig. 3) recording many large sand bodies between 650 and 930 m, in contrast to the dominance of overbank deposits between 360 and 650 m (Fig. 3). The latter also corresponds to the apparent change in amplitudes in the vertical seismic section close to 600 m, far below the Quaternary base (Fig. 2A). Further investigation of higher vertical resolution and facies correlation in a larger area will be necessary to understand if this facies change is the result of climate

changes affecting the sediment supply and transport or was caused by any regional scale basin development.

As structural elements, positive flower structures reaching even the Quaternary strata can be seen in the perpendicular section (Fig. S2); however, not crossing directly the Dévaványa section. These structural elements cause the occurrence of the straight lineation coloured by orange in horizontal slices hampering the interpretations of the channel system, e.g. close to the Dévaványa section at a depth of 1000 m.

The correlation of χ_{LF} and global $\delta^{18}O$ records

The χ_{LF} record of the section (Fig. 3) was compiled by merging of the published Quaternary (Nádor *et al*. 2003; Püspöki *et al*. 2016) and the recently measured Pliocene parts of the borehole. It is presented in combination with lithology, grain-size related wireline logs (GR, Res), the already published palaeomagnetic data (Cooke *et al*. 1979) and the recently measured RGB colour scale. The χ_{LF} record is correlated with the $\delta^{18}O$ record (Lisiecki & Raymo 2005 – LR04) also considering the Pliocene ice-rafted detritus (IRD) records (Allen & Warnke 1991; Jansen *et al*. 2017) and the geomagnetic polarity time scale (Kent 1999).

Immediately below the Matuyama/Gauss boundary, a set of χ_{LF} peaks can be seen in the Gauss Chron. These are analogous with the G2, G4/6, G10 and G18/20 stages (MIS) of the marine isotope stratigraphy. Two moderate but distinct peaks can be seen further down, one in a normal and one in a reverse depth interval, considered as KM2 and M2, respectively. The next distinct peak is at the Gauss/Gilbert magnetic boundary and considered as Gi2, followed by a set of small peaks correlated with Gi4, Gi10/12, Gi14 and Gi20/22.

The following peak at 896–898 m is as significant in its value as those close to the Pliocene–Pleistocene boundary. Considering its very high χ_{LF} value and normal polarity together with the significant secondary peak below, this peak can be correlated with Si4 and the normal polarity section of the core with Sidufjall, instead of Cochiti. Accepting this slight re-interpretation of the normal polarity zone at 870–930 m, the next normal polarity zone at 990–1085 m is the Therva Subchron, which is also confirmed by the two distinct χ_{LF} peaks analogous with T4 and T8 MISs. The significant Pliocene glaciations, discussed by De Schepper *et al*. (2014), are also labelled in Fig. 3 to faciliate the interpretation of the correlated χ_{LF} peaks.

A consequence of this correlation is that contrary to former interpretations (Cooke *et al*. 1979; Elston *et al*. 1994; Magyar & Sztanó 2008), the Cochiti and Nunivak normal polarity subchrons are missing from the Dévaványa section. This is most probably a result of the lateral erosion of the large channel belts recorded by wireline logs in the 789–815 and 828–848 m depth intervals. Short normal polarity zones can be seen at the sites of the Cochiti and Nunivak subchrons, right at the base of these channel complexes, which supports their possible denudation.

Magnetic mineralogy based on SEM investigations

To describe the magnetic mineralogy of the Pliocene section, the separated magnetic phase of a set of samples was investigated by SEM. The sampled χ_{LF} peaks (Fig. 3) were the Quaternary MIS 98 (Fig. 4A, measured points 1, 2), and the Pliocene G4/6 (Fig. 4B–D, mp. 3–9), G18/20 (Fig. 4D–F, mp. 10–12), M2 (Fig. 4G, mp. 13, 14), Gi2 (Fig. 4H, I, mp. 15, 16), Gi10/12 (Fig. 4J, mp. 17, 18), Si4 of special focus (Fig. 4K–Q, mp. 19–31) and Si6 (Fig. 4R–T, mp. 32–37) (Table 1).

The main component is the group of rounded octahedrons of 20–100 microns (Fig. 4A, C–F, J, N–S). This population of grains was transported as bed load and is frequently characterized by exsolution structures of titanomagnetite (Fig. 4D, F, N–S) similarly to the Quaternary samples (Püspöki *et al*. 2016: fig. 6L–N). In a set of grains, the difference between the exsolution lamina and residual cores was measured (mp11, 12, 22, 23, 26, 27, 29, 30, 35, 36). These large octahedrons are very sensitive to the physical decomposition due to the existence of the exsolution lamina.

Another element is the group of idiomorphic magnetite octahedrons of 5–10 microns (Fig. 4B, G–J, T). These grains were transported in suspension or partly as inclusions and thus have kept their original shape; moreover, exsolution structures enhancing physical decomposition were not observed in these grains.

The third type is the group of very small grains of ≤2 microns. These grains are partly idiomorphic octahedrons perhaps transported as inclusions (Fig. 4A, L) and are partly fragments originating from exsolution structures of large octahedrons (Fig. 4K, M). These very small particles can occur in channel deposits (Fig. 4A), but are especially frequent in overbank deposits (Fig. 4K–M). The sample pair from χ_{LF} peak Si4, the lower (898.25 m) representing a channel deposit (Fig. 4O–Q) and the upper (896.0 m) representing the directly overlying overbank setting (Fig. 4K–N), indicates that the source of the <2-micron fragments in the flood-plain is the physically decomposed bed load of the nearby channel.

Ferrimagnetic content and magnetic granulometry

To describe the contributions of ferri- and paramagnetic fractions to the χ_{LF} values, hysteresis investigations were performed as an accepted method used generally in mineralogical investigations (e.g. Dunlop & Özdemir 1997; Leonhardt 2006; Paterson *et al*. 2018) and also in analysis of Quaternary sediments (e.g. Deng *et al*. 2004; Zan *et al*. 2010; Chen *et al*. 2012).

The recently considered Pliocene samples (Fig. 3) were measured (Fig. 5A–C, Tables 2, 3) and compared to the

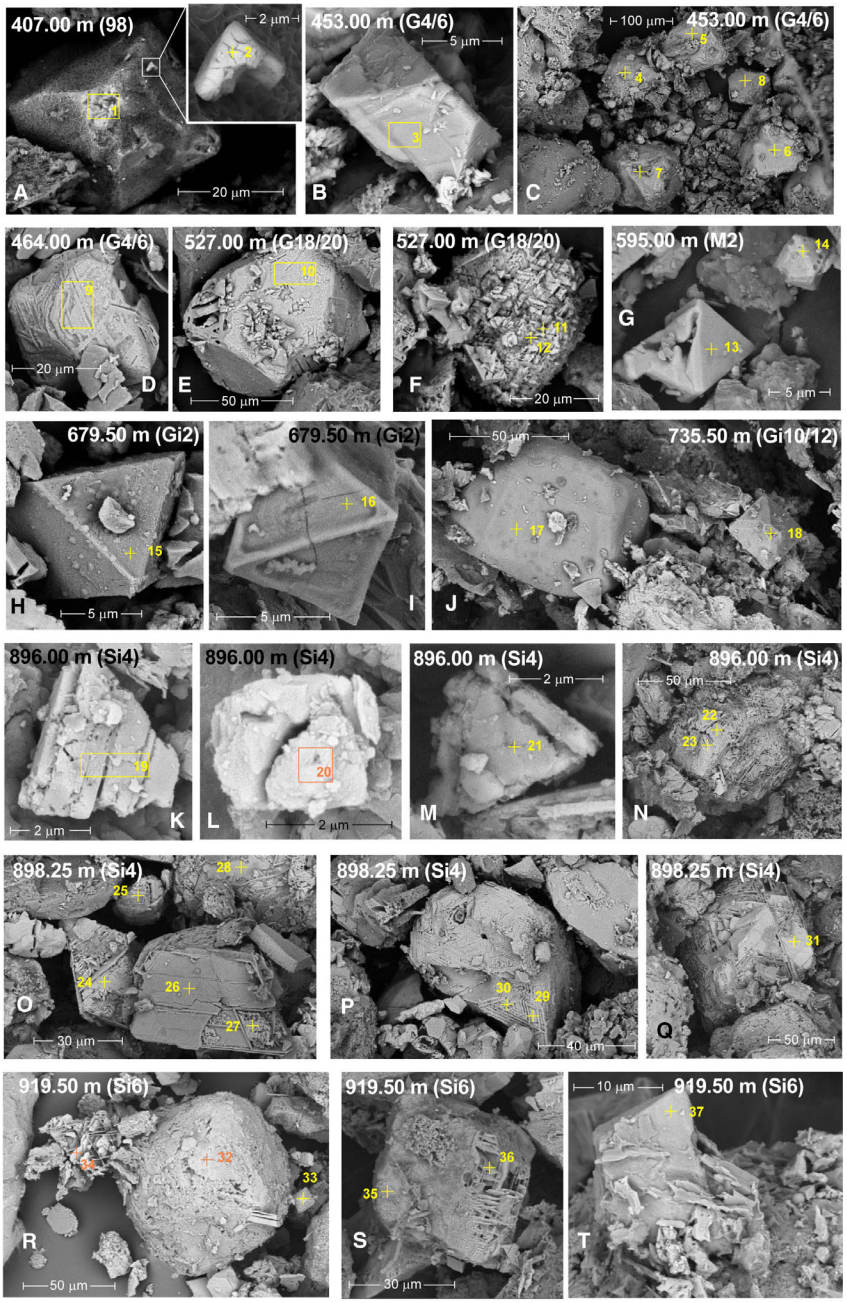

Fig. 4. Scanning electron microscope images of selected magnetic grains. The first number refers to the depth of the sample in metres, the second label (in parentheses) indicates the interpreted stratigraphical position (Fig. 3). Numbered rectangles and crosses of yellow colour are the measurement points. A. 407.00 m, B. 453.00 with measured point 3, C. 453.00 m with measured points from 4 to 8, D. 464.00 m, E. 527.00 m with measured point 10, F. 527.00 m with measured points 11 and 12, G. 595.00 m, H. 679.50 m with measured point 15, I. 679.50 m with measured point 16, J. 735.50 m, K. 896.00 m with measured point 19, L. 896.00 m with measured point 20, M. 896.00 m with measured point 21, N. 896.00 m with measured points 22 and 23, O. 898.25 m with measured points from 24 to 28, P. 898.25 m with measured points 29 and 30, Q. 898.25 m with measured point 31, R. 919.50 m with measured points from 32 to 34, S. 919.50 m with measured points 35 and 36, T. 919.50 m with measured point 37. For the geochemical content see Table 1, for the sedimentological interpretation of the focused and measured grains see the text.

already published samples of nearby Quaternary sections. The volume ratio of the FM component (c_v^{FM}) was calculated according to the equations used in these Quaternary sections (Püspöki *et al.* 2023). The susceptibility of the FM component χ^{FM} is of the order of magnitude of 10^{-2} emu g^{-1} Oe^{-1}. Calculating with magnetite, which was established by SEM investigations of the Pliocene section (Fig. 4), the c_v^{FM} and χ_{LF} values present a reliable linear correlation of $R^2 = 0.98$ (Fig. 5D). Thus, based on the hysteresis data, the variation in c^{FM} is reflected in, and can be estimated from, the variation in χ_{LF}, and the χ_{LF} peaks are driven by

Table 1. Chemical composition (mass percent) of the selected magnetic particles (for the space and form of the grains see Fig. 4). The numbers in italics refer to measurement-pairs presenting the process and rate of exsolution.

Depth (m)	Meas. point	C	O	Na	Mg	Al	Si	Ca	Ti	Fe	Mn	Grain size (μm)	Maintenance	Crystallography
407.00	1	1.26	31.99	0.14	0.43	1.66	1.61	0.00	6.62	56.29	0.00	40	Idiomorphic	
407.00	2	3.42	17.18	0.34	0.22	3.03	4.33	0.00	10.69	60.79	0.00	3	Fragment	
453.00	3	1.43	10.2	0.00	0.00	0.92	1.77	0.38	19.37	65.93	0.00	5	Idiomorphic	Twins
454.00	4	0.42	31.1	0.00	0.28	2.78	6.33	0.37	16.08	42.64	0.00	100	Rounded	
455.00	5	1.06	31.15	0.11	1.15	1.62	1.31	0.00	26.33	37.27	0.00	100	Rounded	
456.00	6	2.04	27.68	0.00	0.09	0.92	2.9	0.34	1.62	64.41	0.00	100	Rounded	
457.00	7	2.03	15.65	0.43	0.38	3.19	5.77	0.00	3.55	69.00	0.00	100	Rounded	
458.00	8	0.00	23.48	0.00	0.00	0.92	2.67	0.66	53.70	18.57	0.00	80	Rounded	
464.00	9	1.52	39.35	0.45	0.69	2.58	4.20	0.00	2.92	48.29	0.00	40	Idiomorphic	Exsoluted
527.00	10	1.87	17.06	0.00	0.21	0.71	0.72	0.00	9.22	70.21	0.00	100	Idiomorphic	Exsoluted
527.00	11	1.61	11.08	0.00	0.31	0.74	0.48	0.00	*10.10*	*75.68*	0.00	30	Rounded	Exs_core
527.00	12	1.23	7.86	0.00	0.10	0.57	0.71	1.99	*15.00*	*72.54*	0.00	30	Rounded	Exs_lamella
595.00	13	0.45	2.83	0.00	0.00	0.53	2.14	0.00	12.24	81.81	0.00	10	Idiomorphic	
595.00	14	0.21	1.54	0.00	0.04	0.34	1.16	0.00	4.42	92.29	0.00	5	Idiomorphic	
679.50	15	3.43	43.29	0.00	0.54	0.97	0.44	0.00	15.23	36.10	0.00	10	Idiomorphic	
679.50	16	4.92	38.59	0.00	1.70	2.26	0.37	0.00	7.69	44.47	0.00	6	Idiomorphic	
735.50	17	7.37	40.55	0.00	1.71	2.36	0.55	0.00	6.92	40.54	0.00	100	Rounded	
735.50	18	3.09	51.16	0.00	0.29	1.46	1.25	0.00	4.55	38.20	0.00	20	Idiomorphic	
896.00	19	4.06	47.16	0.00	0.78	0.57	0.84	1.31	4.64	40.64	0.00	4	Fragment	Exsoluted
896.00	20	4.89	43.35	0.00	0.00	1.21	0.88	1.46	0.00	48.21	0.00	2	Idiomorphic	
896.00	21	0.63	10.68	0.00	0.38	1.72	4.99	0.00	19.77	61.83	0.00	4	Fragment	Exsoluted
896.00	22	2.13	49.77	0.00	0.46	2.26	2.80	0.00	*19.97*	*22.61*	0.00	100	Fragment	Exs_lamella
896.00	23	2.60	51.49	0.14	0.54	1.54	0.48	0.00	*14.37*	*28.84*	0.00	100	Fragment	Exs_core
898.25	24	0.41	2.30	0.00	0.02	0.36	0.44	0.00	1.89	94.58	0.00	30	Idiomorphic	Exsoluted
898.25	25	0.00	40.20	0.00	1.77	1.20	2.81	0.00	27.61	26.41	0.00	15	Rounded	Exsoluted
898.25	26	7.22	16.60	0.00	0.85	0.31	0.69	0.00	*39.18*	*23.14*	12.01	50	Fragment	Exs_lamella
898.25	27	0.35	7.39	0.00	0.00	0.65	1.10	0.00	*2.27*	*88.24*	0.00	50	Fragment	Exs_core
898.25	28	2.17	38.30	0.00	1.06	0.36	0.71	0.00	27.13	30.27	0.00	50	Fragment	Exsoluted
898.25	29	0.98	7.85	0.00	0.21	0.82	0.91	0.00	*6.10*	*83.13*	0.00	80	Fragment	Exs_core
898.25	30	1.67	23.35	0.00	0.51	0.82	1.01	0.00	*17.25*	*55.39*	0.00	80	Fragment	Exs_lamella
898.25	31	2.46	31.90	0.00	1.41	0.43	0.85	0.00	*26.66*	*36.29*	0.00	100	Rounded	Exsoluted
919.50	32	3.35	47.29	0.14	0.88	2.85	3.21	0.59	*13.45*	*28.24*	0.00	100	Rounded	Exsoluted
919.50	33	0.82	49.80	0.00	0.20	1.43	2.05	0.00	*10.47*	*35.23*	0.00	10	Idiomorphic	
919.50	34	0.88	8.11	0.00	0.59	0.66	1.25	0.00	*25.58*	*58.05*	4.88	50	Fragment	Exsoluted
919.50	35	0.84	39.28	0.00	1.50	1.29	1.12	0.00	*11.87*	*44.10*	0.00	50	Rounded	Exs_core
919.50	36	3.89	49.81	0.00	2.26	0.66	1.11	0.3	*17.51*	*24.46*	0.00	50	Rounded	Exs_lamella
919.50	37	3.38	50.01	0.62	0.75	2.83	5.70	0.00	*6.02*	*30.69*	0.00	10	Idiomorphic	

increases in c_v^{FM}, superimposed on a relatively constant paramagnetic background.

Frequency dependent susceptibility (χ_{FD}%) measurements were performed to investigate the superparamagnetic character of the susceptibility maxima. The measurement conditions allowed reliable measurements above $\sim 60 \times 10^{-8}\,m^3\,kg^{-1}$, thus a selected set of 48 samples above this value, including the samples of the correlated χ_{LF} maxima studied also by SEM and hysteresis investigations, was measured. The χ_{FD}% of samples range between −2.5 and 6.7% independently of the χ_{LF} and present a reliable normal distribution (Fig. 5E, F). The only exception is the sample at 896 m, the high χ_{FD} value (11.5%) of which reflects its partly superparamagnetic character, possibly due to the mechanical segregation of grains when transported to the flood-plain (Fig. S1D). A relatively high, 0.37/1.121 ratio of superparamagnetic/ferrimagnetic content of the 896 m sample is also revealed by the hysteresis investigation (Fig. 5G; for the method of calculation see Data S1).

Time series analysis

Based on the stratigraphical correlation (Fig. 3), the section was changed into a time-domain, and spectra of the different proxies were investigated (Fig. 6). Since the re-scaling was performed based on paleomagnetic data in combination with χ_{LF} peaks, the spectrum of colour parameters was not affected artificially by the re-scaling, thus it can confirm the resulted age model and can complete at the same time the facies interpretation (Weedon 2003).

The χ_{LF} of the Plio–Pleistocene time interval (Fig. 6A) reveal apparent ~100-ka and moderate but statistically also relevant ~41-ka frequencies indicating the dominance of eccentricity cycles and occurrence of obliquity cycles. A closer view of the spectrum at very low

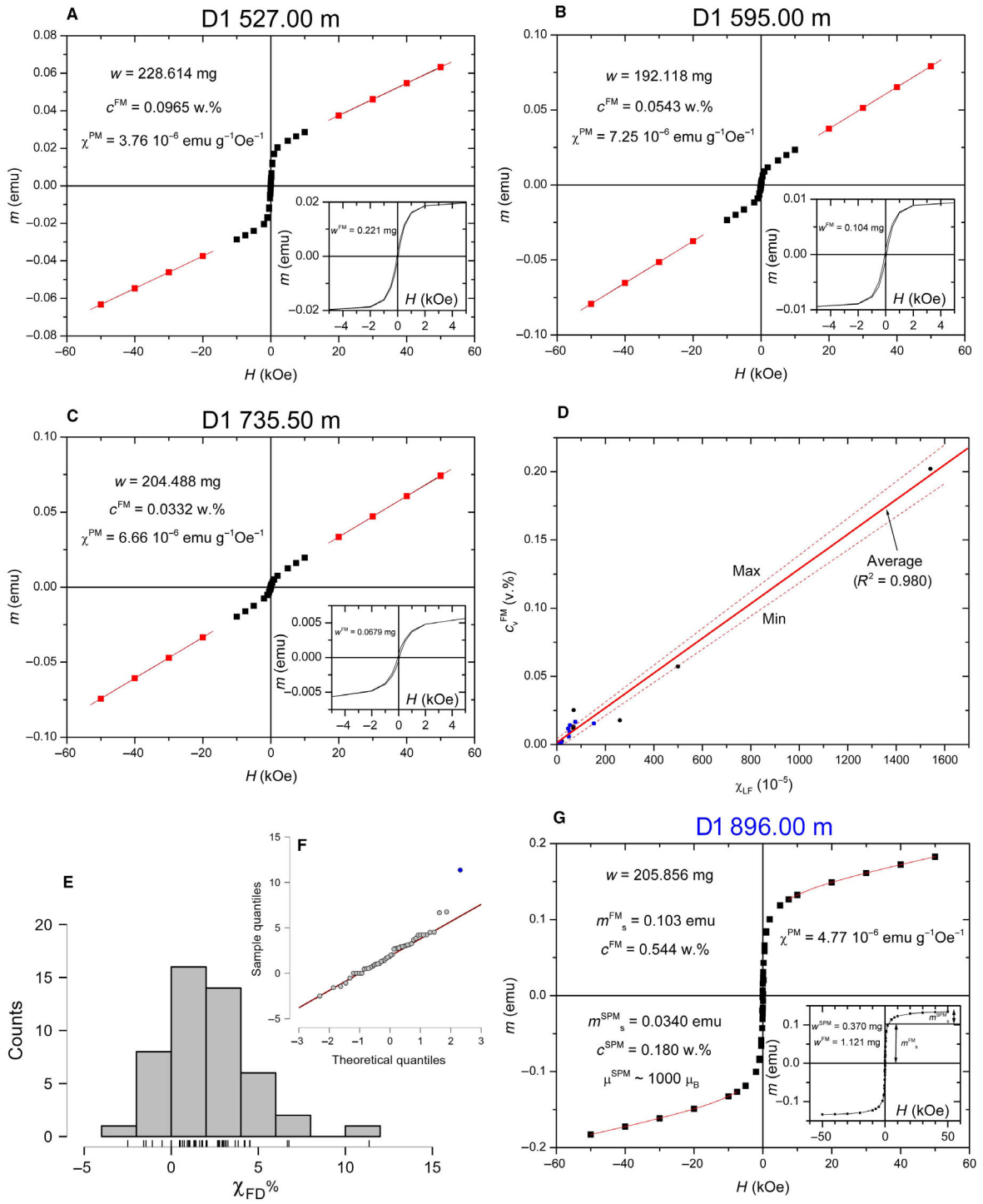

Fig. 5. Ferrimagnetic content and magnetic granulometry of the Pliocene samples in the Dévaványa section. A–C. Magnetic hysteresis curves (magnetic moment vs. magnetic field) for representative samples of given depth (in metres), the insets present magnetic hysteresis of the ferrimagnetic magnetite contained in the sample after eliminating the PM contribution. w and w^{FM} are sample mass and mass of the FM (magnetite) component, respectively. c^{FM} is weight (mass) concentration of the FM component. χ^{PM} is susceptibility of the paramagnetic component. D. Volume concentration of magnetite (c_v^{FM}) as a function of low field magnetic susceptibility (χ_{LF}) for the Pliocene (blue points) and already published Quaternary (black points) samples. The points are the measured values, the solid line is a linear fit to the data, the dashed lines show the upper and lower limits of the values obtained from the error margins of the fit. E. Distribution of frequency dependent magnetic susceptibility of 48 samples from the Dévaványa section. F. QQ plot of the same sample set. G. Magnetic hysteresis curve of the outlier sample (blue point in the QQ plot). w, w^{FM} and w^{SPM} are sample mass, mass of the FM (magnetite) and SPM (magnetite) component, respectively. c^{FM} and c^{SPM} are weight (mass) concentrations of the FM and SPM component, respectively. m_s^{FM} and m_s^{SPM} are saturation magnetic moments of the FM and SPM component, respectively. μ is the average magnetic moment of the SPM clusters.

Table 2. Parameters deduced from the hysteresis curves for the selected samples (χ^{PM} and ρ^{PM} are susceptibility and density of sand, respectively, c^{FM} and c_v^{FM} are mass and volume concentration of magnetite, respectively, and H_c is coercive field).

Sample no. and depth (m)	χ^{PM} (10^{-6} emu g^{-1} Oe^{-1} or 10^{-8} m^3 kg^{-1})	ρ^{PM} (g cm^{-3})	c^{FM} (w.%)	c_v^{FM} (v.%)	H_c (Oe)
D1 453.00	2.72/3.42	0.9	0.09	0.0155	60
D1 486.00	2.19/2.76	0.902	0.00992	0.00171	50
D1 527.00	3.76/4.73	0.9	0.0965	0.0166	45
D1 595.00	7.25/9.11	0.886	0.0543	0.00919	60
D1 735.50	6.66/8.36	0.924	0.0332	0.00586	60
D1 898.25	2.91/3.65	0.929	0.08	0.0142	50
D1 919.50	2.86/3.59	0.984	0.0621	0.0117	45
D1 931.00	8.36/10.50	0.957	0.00991	0.00181	80

frequencies (Fig. 6B) suggests the possibility of cycles of millions of years; however, the resolution of the spectrum is not sufficient to determine the precise lengths of these periods. The spectrum of the pre-Quaternary time interval (>2500 ka; Fig. 6C) reveals the dominance of the ~41-ka cycles. Marked occurrence of obliquity cycles was also reported in Quaternary fluvial deposits representing a source-proximal distributary channel pattern (Püspöki *et al.* 2023), but in that case the occurrence of the high frequency cycles was proven to be the results of the joint effect of sedimentary and mineralogical processes. However, Dévaványa represents a source-distal position, and based on the 3D seismic data (Fig. 2) the channel pattern does not refer to a distributary system. Moreover, the grain-size related wireline logs do not reveal any regular cyclicity in the sedimentological processes. Thus, the obliquity cycles in the pre-Quaternary time interval can be explained as resulting from the Pliocene climate conditions and the high sediment accumulation rate during the Pliocene Epoch relative to that during the Pleistocene.

Somewhat similar spectral characteristics can be seen in the red component of the colour scale, revealing almost ~100-ka cycles in the entire Plio–Pleistocene succession (Fig. 6D) and ~41-ka cycles (CL = 95%) during the Pliocene (Fig. 6E). However, in this case the Pliocene time interval is also characterized by 18–22 ka precession cycles (CL = 99%). This regular cyclicity of colour reveals that the 'variegated' appearance of the Pliocene Zagyva Formation – formerly referred to as 'Nagyalföld Variegated Clay Formation' – records regular couplets of overbank fines and palaeosols of various maturity. They are controlled by obliquity and precession principally through changes in flood frequency or rearrangements of distal and proximal floodplains, among other factors.

Variation in time domain and comparison with orbital solutions

To investigate the temporal relationship between permafrost conditions and solar radiation, the Pliocene–Pleistocene χ_{LF} record in the time domain was compared with insolation but calculated in this case using the average of the related catchment area (Fig. 1), i.e. 47°N (Fig. 7). Eccentricity (ECC) is also plotted as the dominant orbital component affecting the long-term modulation of insolation.

At first glance, the apparent χ_{LF} maxima coincide closely with the anomalously attenuated 'Plio1' and 'Plio–Pleistocene' ~405-ka terms of ECC and insolation. This attenuation seems to be the result of the attenuation of the ~100-ka ECC cycles. As the ~100-ka frequency is the dominant component in the χ_{LF} spectrum (Fig. 6A), these regular attenuations of the ~100-ka cycles were particularly investigated.

In the first step, band pass (Gaussian) filters were applied at frequency = 0.01 1 ka^{-1} both on the proxies (χ_{LF} and $\delta^{18}O$ the latter as a correlation target) and on the considered solutions. The bandwidth was defined as bw = 0.002 1 ka^{-1}, but in the case of ECC bw = 0.001 and 0.002 1 ka^{-1} were also used. To express the amplitude modulation of the 100-ka cycles, envelopes of the filtered records were generated (Hilbert transformation). The ECC filtered by bandwidth = 0.002 1 ka^{-1} expresses the relative differences between the unique 405-ka terms, while that filtered by bw = 0.001 1 ka^{-1} emphasizes the long-term trend of amplitude modulation.

Before any comparison of the amplitude modulations in the proxies and orbital solutions, the reliability of the filtered χ_{LF} signal was tested by comparing the envelope

Table 3. Measured values of χ_{LF} (2nd column: dimensionless volume susceptibility; 4th column: mass susceptibility), ρ_{av} average density, χ^{FM} susceptibility of magnetite, and H_c coercive field.

Sample no. and depth (m)	χ_{LF} (10^{-5}) (SI)	ρ_{av} (g cm^{-3})	χ_{LF} (10^{-5} emu g^{-1} Oe^{-1} or 10^{-8} m^3 kg^{-1})	χ^{FM} (10^{-2} emu g^{-1} Oe^{-1})	H_c (Oe)
D1 453.00	152.4	0.901	13.5/169	14.70	60
D1 486.00	11.49	0.902	1.01/12.7	8.01	50
D1 527.00	76.13	0.9	6.73/84.6	6.58	45
D1 595.00	52.45	0.887	4.71/59.2	7.33	60
D1 735.50	49.55	0.924	4.27/53.6	10.80	60
D1 898.25	53.86	0.93	4.61/57.9	5.40	50
D1 919.50	46.52	0.984	3.76/47.3	5.59	45
D1 931.00	18.82	0.957	1.57/19.7	7.37	80

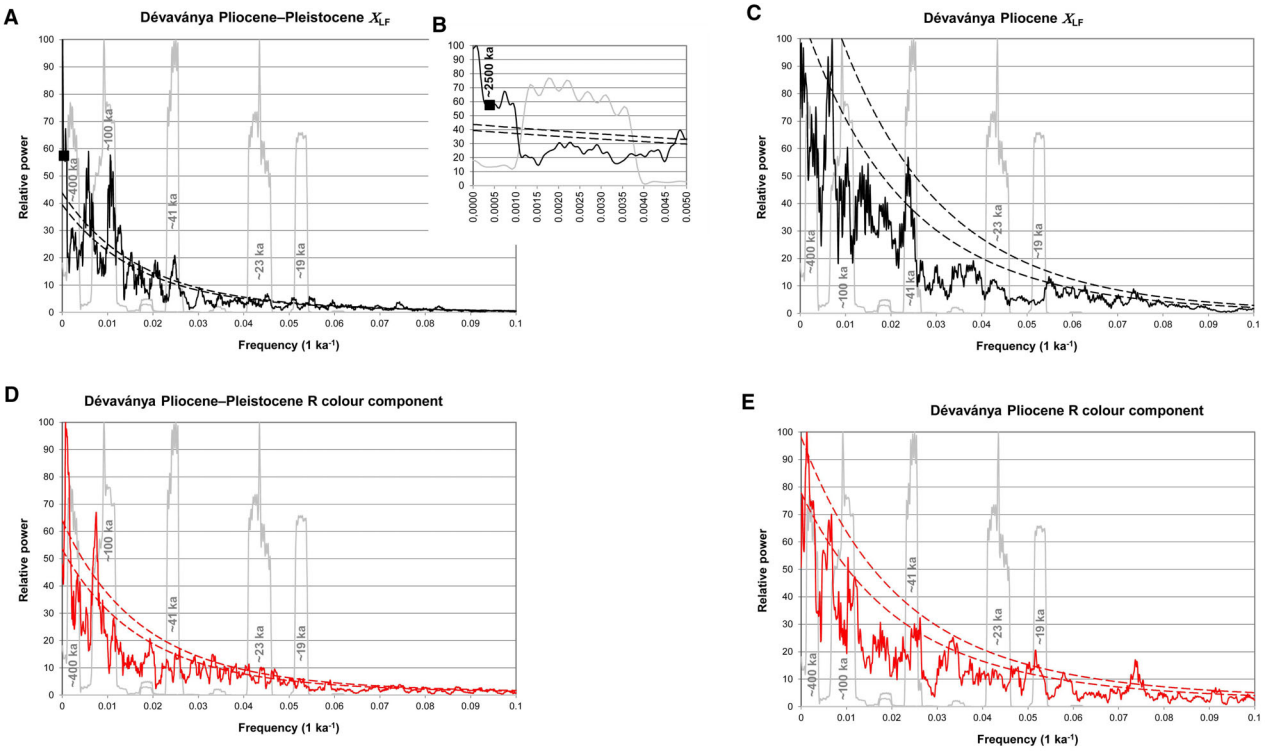

Fig. 6. MTM spectra of the magnetic susceptibility and colour of samples. A. Spectrum of the Plio–Pleistocene χ_{LF} record. B. Enlarged part of (A) at very low frequencies. C. Spectrum of the Pliocene χ_{LF} record. D. Spectrum of the R component in the colour scale considering the entire Plio–Pleistocene time interval. E. Spectrum of the R component in the colour scale considering the Pliocene time interval. The grey spectra are of La2004 orbital solutions (Laskar *et al.* 2004).

of 100-ka cycles with the simple average values calculated using 100-ka intervals. The similarity of the averaged χ_{LF} curve and the envelope of the filtered insolation curve indicates that the envelope is reliable, i.e. the filtered signal reflects the real content of the investigated proxy record.

The first important finding from the comparison of envelopes is that not only do the 'Plio1' and 'Plio–Pleistocene' 405-ka terms coincide with increased χ_{LF} values, but the moderately attenuated 'Plei5' and 'Plei6' 405-ka terms of the last 800 ka do as well. Indeed, these data suggest that – considering only the predicted orbital changes and the Milankovitch theory – the Earth will be faced with very extensive permafrost development in the 'forthcoming' 405-ka term.

The Si4 χ_{LF} maximum seems to occur prior to and thus out of phase relative to the start of 'Plio1'. However, it must be considered that the age of Si4 in the LR04 as the correlation target is constrained by the top of the Sidufjall Subchron (Fig. 3), determined by orbital tuning (Hilgen 1991; Kent 1999). In contrast, either because of the 'top Cochiti problem' of about 150–180 ka (Cande & Kent 1995), or the scarceness of data between the Nunivak and Sidufjall subchrons, the age of top Sidufjall may have some uncertainty. From this perspective, the $\delta^{18}O$ record of the ODP 659 site (Fig. 1), though not documented palaeomagnetically but tuned by high resolution precession cycles of the dust record (Tiedemann *et al.* 1994: figs 7, 8), could be a promising correlation target. The age of the large heavy isotope anomaly, although it is labelled by the referred authors as NS4 due to the projected palaeomagnetic time scale, is placed at 4700 instead of 4850 ka (Fig. 7). Considering this peak as a correlation target, the outstanding χ_{LF} maximum would occur at 4700 ka, just in phase with 'Plio1'.

An important outcome of the filtering of proxies is that the filtered versions of χ_{LF} and $\delta^{18}O$ are markedly similar; the correlation of their envelopes is high ($R^2 = 0.69$). So, the long-term modulation of the 100-ka cycles is a common feature of the marine global ice volume record and the terrestrial local mid-latitude frost record.

The amplitude modulation of the 100-ka period revealed in the terrestrial proxy was tested by a wavelet analysis of the χ_{LF} record extracting the averaged wavelet power over the 84–119 ka band (Fig. 7). The similarity of the 100-ka filter envelope and the 80–119 ka wavelet power confirms that the filtered signal reflects the real content of the investigated χ_{LF} record.

To analyse the possible effect of seasonal variations and geographical position, i.e. latitude of the catchment area, envelopes of the filtered monthly average insolation curves for the 47°N, 37°N, 57°N, 65°N latitudes were calculated and correlated with the envelope of the filtered

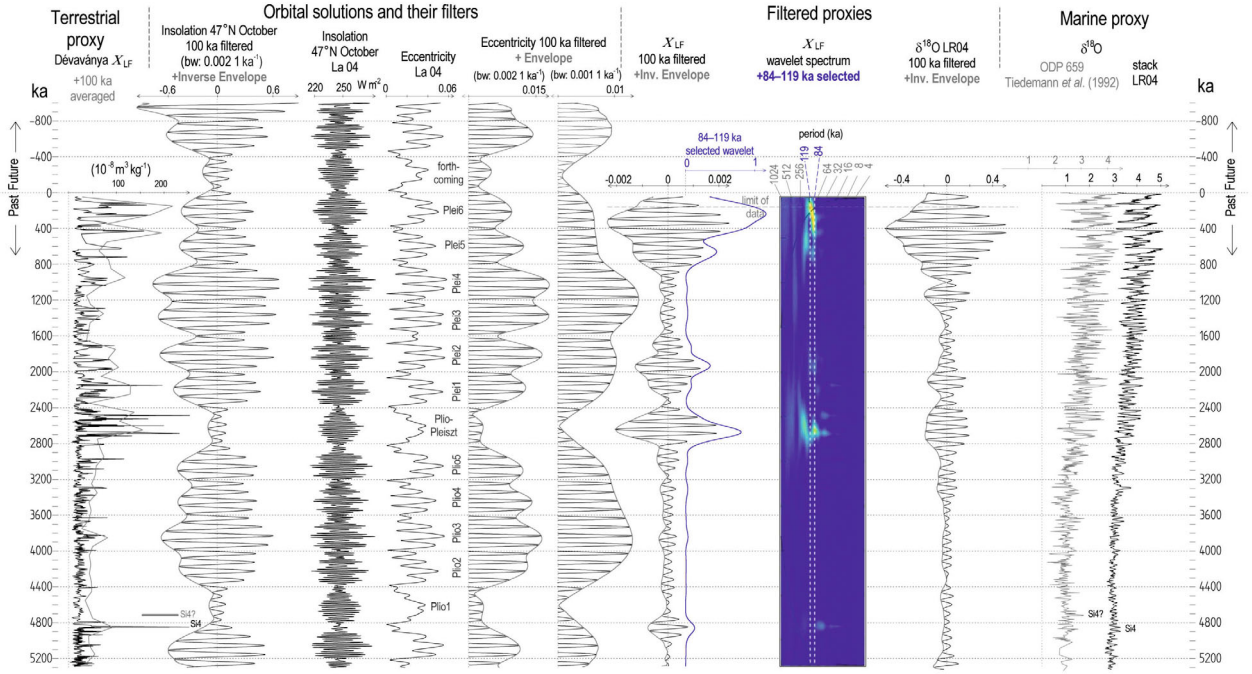

Fig. 7. Comparison of the Dévaványa χ_{LF} record, its 100-ka averaged form and filtered versions (band pass filter fw = 0.01, bw = 0.002 1 ka^{-1}, wavelet scale and averaged wavelet extracted over 84–119 ka band) with those of the marine isotope records (Tiedemann *et al.* 1994; Lisiecki & Raymo 2005) and of orbital solutions, which are eccentricity and 47°N October insolation (180–210° from Vernal Point) (Laskar *et al.* 2004). The filtered curves are enveloped using Hilbert transformation.

χ_{LF} at Dévaványa (Fig. S3). It is important to note that, due to the counter-correlation, that is to the increasing of χ_{LF} with the decreasing of eccentricity amplitude, only the absolute value of the correlation coefficient is relevant. The consequent trend of the correlation coefficients (Fig. 8) indicates that early spring and late autumn months, especially February–March and October–November, have particular importance; moreover, this seasonal dependence may be characteristic throughout the wider temperate zone, regardless of latitude.

Discussion

Fluvial χ_{LF} as a proxy for Pliocene occurrence of mountain permafrost in the Carpathians

The Pliocene fluvial χ_{LF} record presented here resembles the previously published Quaternary sections in its most fundamental characteristics. (i) The magnetic mineralogy (Figs 4, 5A–D, Table 1) revealed in the Pliocene section is very similar to that of the Quaternary section. Magnetite is the dominant mineral with various grain sizes and preservation. (ii) Based on published models (Dearing *et al.* 1996), the value of χ_{FD}% (Fig. 5E, F) indicates only a subdominant proportion of superparamagnetic grains; therefore, the main part of the magnetite must represent detrital material transported from the mountainous hinterland. (iii) Spectral characteristics (Fig. 6) reveal that the local facies variation recorded by the colour changes of the 'variegated clay' is controlled by obliquity and precession cycles, whilst in contrast the χ_{LF} record is affected predominantly by eccentricity. These mineralogical, sedimentological and spectral characteristics together indicate that, similar to the Quaternary sections, the Pliocene χ_{LF} record may also document permafrost conditions in the adjacent mountainous catchment area.

To confirm this possibility, it would be relevant to support the Pliocene fluvial χ_{LF} records with data from timed permafrost regions in the catchment area. However, very similar to ancient glaciations (Ehlers & Gibbard 2007) it is difficult to determine the existence and extent of ancient mountain permafrost zones, since the remnants of the early permafrost have been largely removed by the intensive denudation and more extensive subsequent permafrost advances.

As a consequence of this difficulty, in the case of long-term Quaternary sections the permafrost-related origin of the χ_{LF} record was confirmed by comparison of long-term Quaternary χ_{LF} and ice-rafted detritus (IRD) records (Püspöki *et al.* 2021b), based on the assumption that there is a common climate control on the major terrestrial glaciations and the advances of the mountain permafrost zones. Although the Pliocene IRD data (Fig. 3), due to their incomplete character, are not ideal

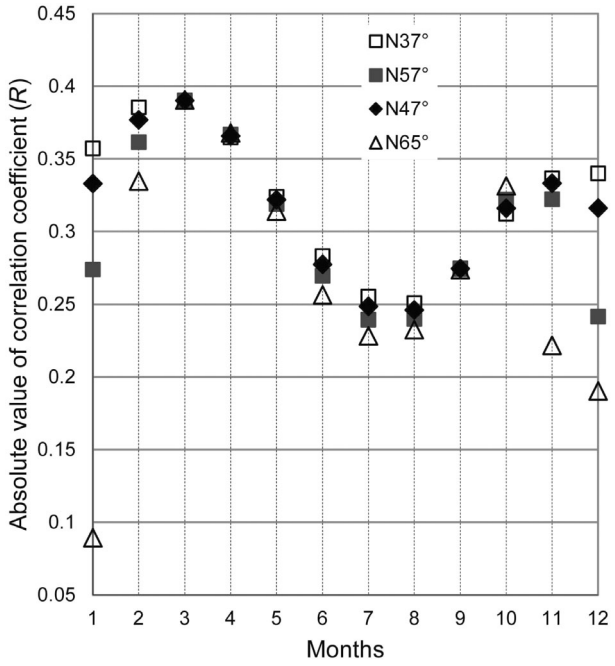

Fig. 8. Correlation coefficients between the envelopes (fw = 0.01, bw = 0.002 1 ka^{-1}) of the χ_{LF} record at Dévaványa and of the monthly average insolation values at latitudes 65°N, 57°N, 47°N, 37°N (for the data and workflow at 47°N see Fig. S2).

for a continuous comparison, the well-documented Pliocene glaciations (De Schepper *et al.* 2014), together with published Pliocene IRD records (Allen & Warnke 1991; Jansen *et al.* 2017) present a reliable temporal coincidence with the maxima of the χ_{LF} record determined here.

This stratigraphical coincidence of χ_{LF} maxima with terrestrial glaciations and glaciations recorded in the $\delta^{18}O$ records (Lisiecki & Raymo 2005) indicates that, similar to the conditions during the Quaternary (Popescu *et al.* 2017), permafrost extensions could occur in the Carpathians that are related to glaciations during the Pliocene Epoch (Fig. 3). These genetically interpreted and stratigraphically reliable Plio–Pleistocene data may be important when aging and interpreting denudation chronologies in Romania (Bălteanu *et al.* 1998) or in larger areas of the Carpathians (Minár *et al.* 2004; Aherwar *et al.* 2024) or the Alps (Wapenhans *et al.* 2024).

The nature and advantages of a long-term terrestrial frost record

The effects of insolation may be very complex, for example on global wind and sea current systems and thus on spatio-temporal changes of the climatic regions. However, this is not the case in a local mountainous catchment, the surface temperature of which is directly determined by the local insolation. Thus, the Pliocene–Pleistocene χ_{LF} at Dévaványa can really be considered as a record of a thermometer stuck into the soil of the adjacent mountainous catchment and measuring the surface frost throughout 5 000 000 years. More precisely, the value of χ_{LF} is proportional to the spatial extension of the permafrost zone in the attached catchment, that is to the descent of the snowline or permafrost line most likely in harmony with the global changes of ice volume.

The consequent long-term response of permafrost extension to the insolation revealed (Fig. 7) is a novel confirmation of the Milankovitch theory, close to its original study area in the Mid-European alpine region. An important element of the Milankovitch theory is that the expansion of ice is inhibited by hot summers causing the melting of the frozen material. The long-term permafrost record proposed here also emphasize the importance of seasonality; however, considering the outstanding importance of late autumn and early spring (Fig. 8), in a different way, i.e. enhancing the role of the *lengths* of the winters (see below).

Moreover, the long-term character of the record makes it possible to test this statement not only on the Pleistocene high-frequency Milankovitch scale cycles, but on the scale of the long-term Plio–Pleistocene time interval. This long-term character also makes it possible to consider moderate (0.02) amplitude variations of eccentricity, revealing the importance of small but long-lasting modulation in insolation. This may have consequences both on the mode of orbital control, and on the impact of the secular solar system variations on glaciations, considering their chronology and dynamic behaviour.

The nature of orbital control on mountain permafrost development

The regular coincidences of χ_{LF} maxima and 405-ka terms of the attenuated 100-ka ECC cycles suggest that the attenuation of the variations in the autumn and spring seasons is vital in the extension of permafrost in the temperate zone. This seems to offer an explanation for the early Pliocene glaciations during 'Plio1', for the INHG in the 'Plio–Pleistocene' 405-ka term, and for the large glaciations during the 'Plei5' and 'Plei6' 405-ka terms, foreshadowing a possible glaciation in the 'forthcoming' 405-ka term.

One could say that the global mean annual insolation on Earth is not strongly influenced by ECC variations, but this is not the case for seasonal variations. A change of 0.02 in the ECC, which is almost equal to the attenuations of the 100-ka cycles discussed here, can cause a difference of about 6 K (Laskar *et al.* 2011) in the temperature of a season depending on its perihelion vs. aphelion position, which is controlled by precession cycles. So, the revealed seasonality in the χ_{LF} record (Fig. 8), that is the apparent maxima of correlation with the October–November and February–March monthly

insolation, has special importance. In fact, it is the annual build-up and destruction of the snow cover in the catchments of the entire temperate zone (e.g. Marty 2013; Kawase *et al.* 2020) that is controlled by the long-term amplitude modulations of ECC and insolation. This outstanding effect of relatively warm October months is directly observed in modern permafrost regions (e.g. Berwyn 2017; Randazzo *et al.* 2021; Byrne *et al.* 2022). The importance of *lengthened* winters is also supported by the fact that cold winters especially favour permafrost development, while summer heat is only responsible for some increasing depth of the active layer.

The role of seasonality, particularly in the wider regions of the temperate zone, is also confirmed by the revealed latitude-independence (Fig. 8). This independence is the effect of the relief on insolation, since the steepness and direction of slopes in the mountainous catchments considerably overprint the role of geographical latitude in the angle of incidence of solar radiation; thus again, the seasonality remains as the only important factor that is directly controlled by orbital changes.

In short, the mountain permafrost history of the temperate zone is proved to be controlled by the 100-ka cycles of ECC. The increased 100-ka ECC cycles apparently terminate permafrost extensions; thus, if these extremes are present, the permafrost regions are very limited or almost disappear. If these 100-ka ECC extremes are attenuated, this allows the 100-ka permafrost cycles to occur throughout wide regions of the temperate zone.

This importance of autumnal and vernal months could suggest that the importance of attenuation of 100-ka ECC cycles emphasized here is relevant only in the temperate zone characterized by four seasons, but this exclusiveness is far from unambiguous. It is worth noting that the 100-ka ECC cycles are also well documented in ice-cores of polar regions (e.g. Petit *et al.* 1999; Johnsen *et al.* 2001; Jouzel *et al.* 2007) and thus can be affected also by these attenuations. The insolation during February–April and September–October in Greenland and Antarctica is similarly modulated by eccentricity (Fig. S4); however, considering that the temperature is permanently below freezing point, the way that orbital changes impact on ice growth is certainly different. They are presumably associated with precipitation, which is supported by the fact that the surface height change reaches its maximum during September and April in Greenland (Castellani *et al.* 2015: fig. 4), and the area-integrated precipitation in Antarctica reaches its maximum in March–May (Lenaerts *et al.* 2016: figs 7, 8).

Secular variations of the solar system – the chronology and dynamics of glaciations

The similarity of 100-ka filtered Plio–Pleistocene χ_{LF} and $\delta^{18}O$ records (Fig. 7) revealed here confirms the already discussed common climate control on the major glaciations and the regular advances of the mountain permafrost zones (Püspöki *et al.* 2021a). This allows the consideration of the two variables, i.e. the $\delta^{18}O$ recording global ice volume and χ_{LF} recording the permanent terrestrial frost as two independent responses on the same set of climatic variations. Based on this similarity, a joint interpretation of mountain permafrost and glaciation history is discussed below in the light of long-term orbital variations.

The long-term amplitude modulation of the 100-ka cycles is determined by secular variations of the solar system. The approximately 2.4 Ma g_4–g_3 (Mars–Earth) cycle superimposed on the 405 ka g_2–g_5 (Venus–Jupiter) terms is well known (Laskar *et al.* 2011); however, during the last 14 Ma this 2.4-Ma cycle has been a regular variation of 2.0 and 2.8 Ma cycles practically. Although the solar system models have some uncertainty due to its chaotic behaviour (Laskar 1989), the resolution of this last 14 Ma is almost the same in different models (Laskar *et al.* 1993, 2004, 2011) indicating that the models, established on the recent state of the solar system, are reliable for this time period.

The Pliocene–Pleistocene interval starts with an attenuated 405-ka term (Plio1; Fig. 7) that is followed by four regular 405-ka terms (Plio2–5). The INHG at the Pliocene–Pleistocene transition coincides well with a subsequent attenuated 405-ka term that is followed again by four regular 405-ka terms (Plei1–4). However, before the onset of the 'forthcoming' attenuated 405-ka term, two additional 405-ka terms of moderate attenuation (Plei5–6) are inserted, coinciding with the large glaciations following the Mid-Pleistocene Transition.

The Mid-Pleistocene Transition (Head & Gibbard 2005) is also characterized by the shift of frequency from 41 to 100-ka cycles that has been observed on several occasions in the marine $\delta^{18}O$ record (e.g. Hays *et al.* 1976; Ruddiman *et al.* 1986; Raymo *et al.* 1989). In the absence of any apparent frequency change of the orbital parameters, the interpretations frequently considered the possible effect of the difference in latitudes at which ice sheets were formed (e.g. Clemens *et al.* 1996, reviewed by Weedon 2003). In these models, the obliquity signal is usually considered as being of high-latitude origin, while the climatic precession, i.e. eccentricity and precession, dominates low-latitude changes (e.g. Ruddiman & McIntyre 1984). The orbital trigger of the frequency change was debated later and the additional effect of CO_2 (e.g. Berger *et al.* 1999; Hansen *et al.* 2008), together with albedo (Crowley & Hyde 2008), and the alternate effect of precession in the two hemispheres (Raymo *et al.* 2006), were considered (reviewed e.g. by Jouzel & Masson-Delmotte 2010).

The importance of long-term amplitude modulation of 100-ka ECC cycles presented herein enables the interpretation of the Mid-Pleistocene Transition, together with other more limited frequency changes, in the context of orbital variations; but, one should

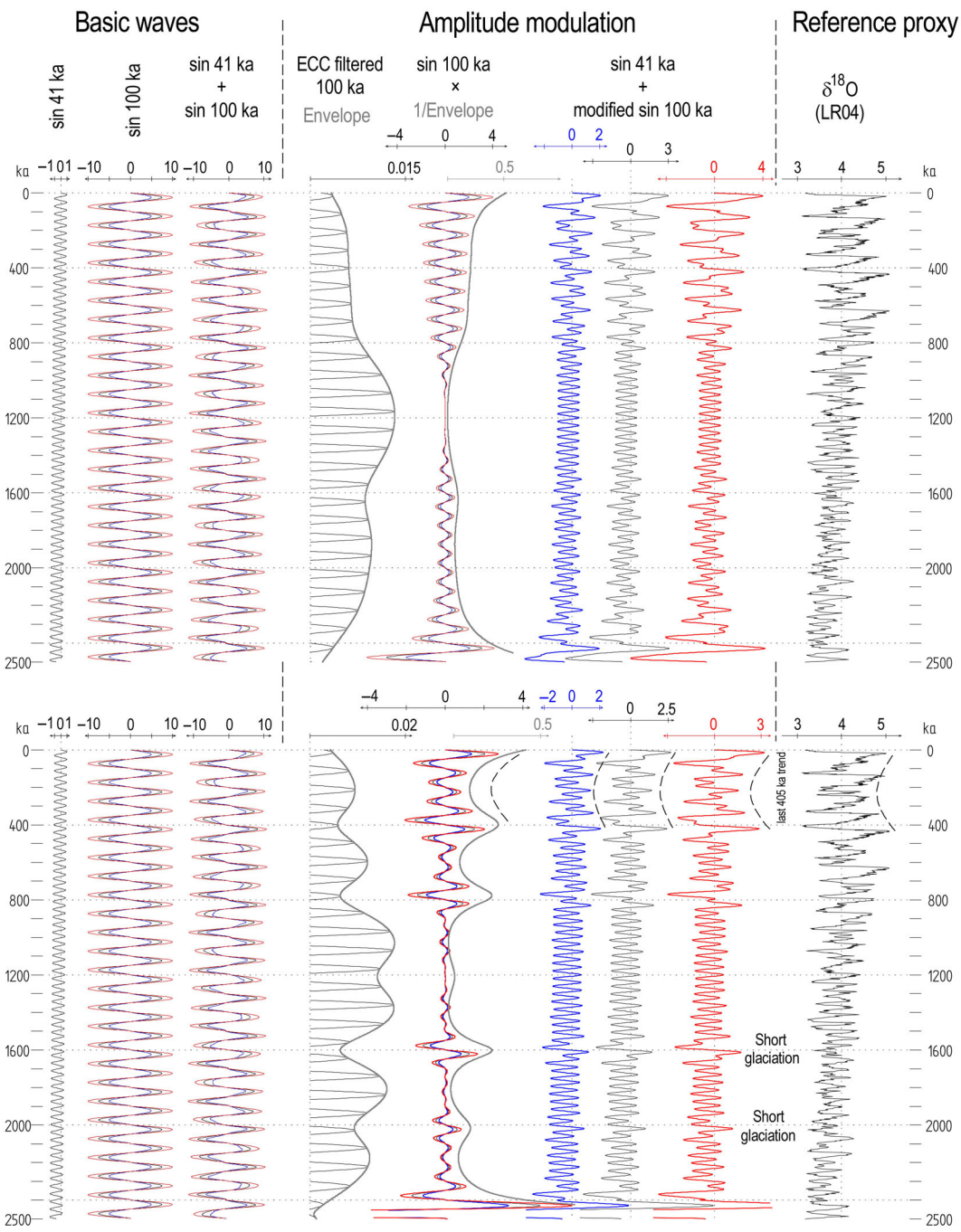

Fig. 9. The eccentricity-derived amplitude modulation model to explain the temporal frequency changes in the Quaternary variation of the global ice volume. Top: the ECC is filtered by bandwidth = 0.001 1 ka^{-1} (frequency = 0.01). Bottom: the ECC is filtered by bandwidth = 0.002 1 ka^{-1} (frequency = 0.01). The colours: blue: 41:100 = 1:5, red: 41:100 = 1:10, black: 41:100 = 1:7.5. The $\delta^{18}O$ is according to Lisiecki and Raymo (2005).

calculate with amplitude-modulation instead of looking for any direct frequency change. The 41-ka shifts of the polar circles drive the seasonality of the polar region. This is a continuous effect, but relatively limited in its area and thus in its amplitude. However, it is reasonable assuming an increaseing trend for it to be, due to the gradual build-up of the polar ice sheet. Contrary to this, the effect of the 100-ka cycles is relevant in wide regions of the temperate zone and possibly of polar regions. It is therefore extended in its area and thus in its amplitude, but it is not continuous because it is strongly modulated by the long-term g_4–g_3 cycles.

Just to illustrate the effect of the proposed amplitude modulation, a simple linearly trended 41-ka sine wave was added to 100-ka sine waves multiplied by 5, 7.5 and 10, respectively, to express

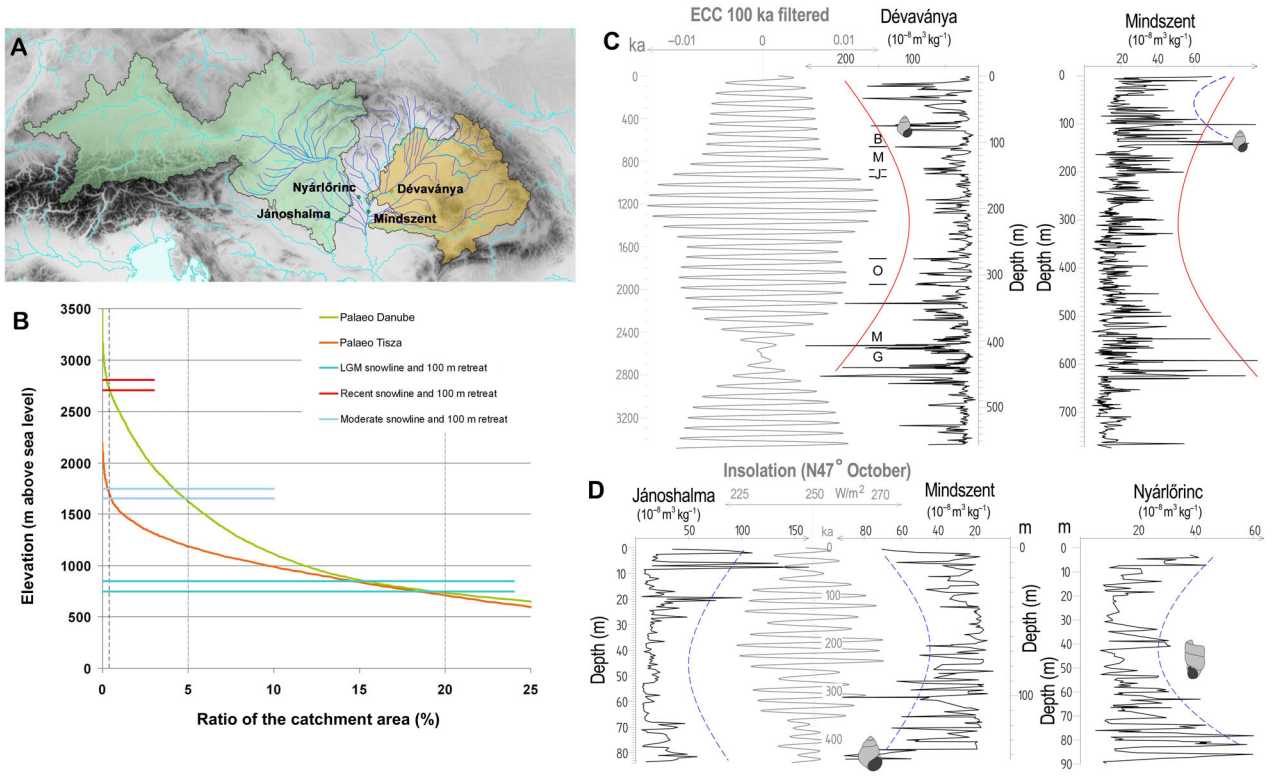

Fig. 10. Comparison and interpretation of χ_{LF} records of different catchment areas and different time scales. A. Geographical sketch of the compared catchment areas and the position of the related borehole sections. B. Hypsometric curves of the compared catchment areas and their relationships to the different altitudes of the snowline. C. Long-term Pleistocene χ_{LF} records of the different catchment areas, together with the filtered eccentricity (fw = 0.01, bw = 0.001 1 ka^{-1}). D. χ_{LF} records of the last 405 ka in the Danube fluvial fan draining the Alps together with the insolation (180–210° from Vernal Point). For the details of Mindszent, Jánoshalma and Nyárlőrinc borehole sections see Püspöki *et al.* (2021a).

the possible ratio of 41-ka and 100-ka ice-sheet variations (Fig. 9). When approaching the 1:5, 1:7.5 or 1:10 ratio of 41-ka vs. 100-ka ice-sheet variations, the 41-ka component was approximated by the area of ice between 65.5N° and 67.9S° latitudes during the Last Glacial Maximum (LGM; *c.* 23–27 ka: Hughes & Gibbard 2014) (Fig. 1), while the 100-ka component was considered as the remaining ice sheet in the temperate zone alone (1:5), or together with polar regions (1:10) and finally a transitional situation (1:7.5) was also considered. Anyhow, the first result is a set of almost monotonous 100-ka waves.

In a second step the amplitude of the 100-ka sine waves was modulated by the long-term variation of the 100-ka ECC cycles (bandwidth = 0.001 1 ka^{-1}) or to be more precise by its reciprocal value due to the counter-correlation between the amplitude of ECC and the length of winters (Fig. 9 top). Adding the modulated 100-ka sine waves to the 41-ka wave, the results resemble the δ^{18}O curve in its most important frequency change, i.e. the change from 41-ka cycles to 100-ka ones in the last 800 ka. The 1:10 ratio seems to be more realistic, suggesting that the amplitude modulation can be a relevant factor in polar regions as well.

When the 100-ka sine waves are modulated by the variation of 100-ka ECC cycles filtered by a twofold bandwidth (0.002 1 ka^{-1}; Fig. 9 bottom) more complex modulations occur. Adding these complex curves to the 41-ka wave, the results resemble the δ^{18}O curve even in its more local characteristics, like the temporal trend of glaciations in the last 405-ka term, and the occurrence of short glaciations between 1500–1700 and 2000–2100 ka.

Assuming the proposed amplitude modulation, the shapes of the resulting curves are sensitive both to the amplitude ratio of the 41 vs. 100 ka cycles and to the filter bandwidth applied to the ECC curve. Supposing dynamic changes of these parameters in time, there is a wide range of possibilities to test in comparison with the δ^{18}O curve, when defining the role of different regions in the variations of the global ice volume. The consideration of high frequency precession cycles in further analyses may result in even more realistic results.

Comparison with another catchment area – the overall trend in Quaternary χ_{LF} records

Comparison with external data was undertaken to test and confirm the interpretation of the Dévaványa χ_{LF}

record. In the absence of globally distributed fluvial χ_{LF} records, it is helpful that the Quaternary fluvial succession of the Pannonian Basin documents χ_{LF} records of two different catchment areas (Fig. 10A). The χ_{LF} record for Dévaványa represents the Carpathians, while that for Mindszent documents the Alps, which are of rather different orography (Fig. 10B). The records have been correlated already (Püspöki *et al.* 2021a, b), and this correlation has been confirmed recently by amino-acid racemization measurements (Nelson *et al.* 2023).

An important factor of the previous correlation was the overall trend occurring in both records, i.e. the gradually increasing set of peaks towards both the upper and lower parts of the Pleistocene and the lack of significant peaks in the middle (Fig. 10C). The interpretation of this feature of the Pannonian Quaternary χ_{LF} records remained ambiguous in earlier studies, and changes in basin geometry together with possible extensions of lacustrine environments were invoked as possible explanations.

The 5-Ma term Pliocene–Pleistocene record at Dévaványa revealed that this trend is simply the direct response of the permafrost development to long-term amplitude variation of the ECC (Fig. 10C). This explanation makes the interpretation of the Pannonian χ_{LF} records easier, and at the same time offers the possibility to compare long-term (2.5 Ma) Pleistocene χ_{LF} records of different fluvial catchments.

The overall upwards increasing trend within the Pliocene–Pleistocene section, especially apparent in the 100-ka filtered version of the χ_{LF} record (Fig. 7), can be explained either by the gradual change in the atmospheric CO_2 level (e.g. Seki *et al.* 2010) or the ongoing Alpine orogeny. However, the apparent similarity of the 2.5-Ma χ_{LF} records of the Alps and Carpathians indicates that the nearly 1500-m altitudinal difference between the Alps and Carpathians did not overprint the overall trends in their Quaternary permafrost records. This could be a potential counter-argument when considering the possible effect of a tectonic uplift on permafrost extension in mountainous regions.

The role of catchment area orography in occurrences of long-term trends in χ_{LF} records

A closer view of the χ_{LF} records focusing on the last 405-ka ECC term reveals a marked difference between the χ_{LF} records of the Alps and Carpathians. Based on malacological data and regional correlations (Püspöki *et al.* 2021a), the upper 80–90 m of the Danube fluvial fan represents the last 450 ka of fluvial load transported from the Alps. The related χ_{LF} records are again characterized by large values on the bottom and top and small values in the middle (Fig. 10D). Considering the insolation curve, this gradual χ_{LF} trend may document the variations in permafrost extension in the Alps during the last 405 ka.

The lack of this 405-ka trend in the Carpathians can be explained by the different catchment topography (Fig. 10B). While during a substantial glaciation like that during the LGM, 20% of both catchments was affected by frost; by about 1000-m retreat of snowline the Carpathian catchment was almost entirely unglaciated, while 5% in the Alps remained impacted by permanent frost. Thus, relative changes during the more limited glaciations within the last 405-ka term cannot be recorded by the Carpathian permafrost.

Conclusions

- The fluvial χ_{LF} profile measured on the 1116-m-long core at Dévaványa is shown to be a quasi-continuous long-term (5 Ma) record of the Plio–Pleistocene permafrost development in the Carpathians. The continuous fluvial character of the sediment sequence is confirmed by the 3D seismic data, the detrital origin of the magnetite is documented by frequency dependent susceptibility measurements, SEM, and hysteresis investigations.
- The χ_{LF} record is correlated to the $\delta^{18}O$ curve (LR04) supported by already published palaeomagnetic data. Considering the colour of the samples, the local fluvial facies changes are characterized by precession and obliquity cycles, but the χ_{LF} indicate the dominance of the 100-ka ECC cycles in the mountainous permafrost events.
- The comparison with orbital solutions revealed that the long-term permafrost variation in the temperate zone is directly driven by the amplitude modulation of the 100-ka ECC cycles. The increased amplitude of the 100-ka cycles, reflecting the shortened winters, terminates the permafrost extensions; thus, if these extremes are present, the permafrost regions are very limited or almost disappear. However, if the 100-ka ECC cycles are attenuated, permanent frost can occur over wide regions of the temperate zone because of the attenuated seasonality and thus lengthened winters.
- The similarity of the 100-ka filtered Plio–Pleistocene χ_{LF} and $\delta^{18}O$ records suggest a common climate control on the regular advancements of the mountain permafrost zones and the major glaciations. Thus, the long-term modulation of 100-ka ECC cycles may be responsible for the early permafrost developments and glaciations during the Pliocene and for the INHG, foreshadowing a strong cooling in the forthcoming 405-ka term. Additionally it enables the explanation of the 41 vs. 100 ka frequency in the Quaternary permafrost and glaciation cycles occurring during the Mid-Pleistocene Transition by an amplitude modulation model. The 41-ka cycles record the regular obliquity-controlled changes close to the polar circles, while 100-ka cycles occur when

the amplitude attenuation of 100-ka ECC cycles enables extended glaciations that – resulting from their large spatial changes – hide the regular 41-ka cycles.

- Because of orographic effects, higher mountains in the fluvial catchment enable higher resolution of permafrost records, thus documenting relative differences in the moderate glaciations by the fluvial χ_{LF} record. Nevertheless, the similarities between the overall trends in Quaternary χ_{LF} records from catchment areas with a 1500-m altitudinal difference questions the significance of tectonic elevations in the extension of permafrost zones.

Acknowledgements. – We thank sincerely John Lewin (Aberystwyth University) for his suggestions on the interpretation of the 3D seismic figure, and Csaba Cserháti and Gergő Vecsei (Debrecen University) for taking the SEM photographs. We also thank the staff of the Paleomagnetic Laboratory under the leadership of Emő Márton for ensuring ideal conditions for the magnetic susceptibility measurements. We are also thankful to Annamária Nádor for enabling us to use the Quaternary χ_{LF} data again. We especially thank the three anonymous reviewers for their critical comments and suggestions.

Author contributions. – ZP planned the research, led the sampling and laboratory measurements and wrote the paper with input from all authors; GM took part in sampling and discussed the text; TF took part in time series interpretations and discussed the related section; LB performed the seismic investigations; LFK undertook the hysteresis investigations and co-wrote the related section and wrote the Supporing Information section text; ET-B conducted the magnetic separations; ZK carried out the mineralogical investigations and discussed the related section; PK performed the wavelet investigations; RWM took part in sampling and discussed the text; ZV took part in sampling and discussed the text, FS wrote the computer coding and discussed the time series analyses and Solar System aspects; ZL took the colour measurements; VM performed the GIS data management and geomorphological analysis; KS collected the comparative data and discussed the results; MR checked the mathematical tests and algorithms and discussed the results; PLG contributed to the manuscript preparation, in particular the global aspects.

Data availability statement. – The data that support the findings of this study are available from the corresponding author upon reasonable request.

References

Aherwar, K., Šujan, M., Chyba, A., Rózsová, B. & Aster Team 2024: Authigenic $^{10}Be/^{9}Be$ dating of the Horná Štubňa river terrace points to the inception of the terrace staircase formation to the next row Turiec Basin (Slovakia) from the middle Pleistocene transition. *Acta Geologica Slovaca 16*, 33–44.

Allen, C. P. & Warnke, D. A. 1991: History of ice rafting at leg 114 sites, Subantarctic/South Atlantic. *In* Ciesielski, P. F., Kristoffersen, Y., Clement, B. & Moore, T. C. (eds.): *Proceedings of the Ocean Drilling Program, Scientific Results 114*, 599–607. Ocean Drilling Program, College Station, TX.

Bălteanu, D., Ielenicz, M. & Popescu, N. 1998: Geomorphology of the Romanian Carpathians – new trends and evolutions. *Studia Geomorphologica Carpatho-Balcanica 32*, 89–109.

Berger, A., Li, X. S. & Loutre, M. F. 1999: Modelling northern hemisphere ice volume over the last 3 Ma. *Quaternary Science Reviews 18*, 1–11.

Berwyn, B. 2017: Thawing Alaska permafrost sends autumn CO_2 emissions surging. *Inside Climate News*, May 8th 2017.

Byrne, B., Liu, J., Yi, Y., Chatterjee, A., Basu, S., Cheng, R., Doughty, R., Chevallier, F., Bowman, K. W., Parazoo, N. C., Crisp, D., Li, X., Xiao, J., Sitch, S., Guenet, B., Deng, F., Johnson, M. S., Philip, S., McGuire, P. C. & Miller, C. E. 2022: Multi-year observations reveal a larger than expected autumn respiration signal across northeast Eurasia. *Biogeosciences 19*, 4779–4799.

Cande, S. C. & Kent, D. V. 1995: Revised calibration of the geomagnetic polarity timescale for the Late Cretaceous and Cenozoic. *Journal of Geophysical Research 100*, 6093–6095.

Castellani, B. B., Shupe, M. D., Hudak, D. R. & Sheppard, B. E. 2015: The annual cycle of snowfall at Summit, Greenland. *Journal of Geophysical Research: Atmospheres 120*, 6654–6668.

Chen, Q., Liu, X. M., Heller, F., Hirt, A. M., Lü, B., Guo, X. L., Mao, X. G., Chen, J. S., Zhao, G. Y., Feng, H. & Guo, H. 2012: Susceptibility variations of multiple origins of loess from the Ily Basin (NW China). *Chinese Science Bulletin 57*, 1844–1855.

Chen, L. M., Zhang, G. L. & Effland, W. R. 2011: Soil characteristic response times and pedogenic thresholds during the 1000-year evolution of a paddy soil chronosequence. *Soil Science Society of America Journal 75*, 1807–1820.

Clemens, S. C., Murray, D. W. & Prell, W. L. 1996: Nonstationary phase of the Plio-Pleistocene Asian Monsoon. *Science 274*, 943–948.

Cooke, H. B. S., Hall, J. M. & Rónai, A. 1979: Paleomagnetic, sedimentary and climatic records from boreholes at Dévaványa and Vésztő, Hungary. *Acta Geologica Hungarica 22*, 89–109.

Cornu, S., Lucas, Y., Lebon, E., Ambrosi, J. P., Luizao, F., Rouiller, J., Bonnay, M. & Neal, C. 1999: Evidence of titanium mobility in soil profiles, Manaus, central Amazonia. *Geoderma 91*, 281–295.

Cremonese, E., Gruber, S., Phillips, M., Pogliotti, P., Boeckli, L., Noetzli, J., Suter, C., Bodin, X., Crepaz, A., Kellerer-Pirklbauer, A., Lang, K., Letey, S., Mair, V., Morra di Cella, U., Ravanel, L., Scapozza, C., Seppi, R. & Zischg, A. 2011: An inventory of permafrost evidence for the European Alps. *The Cryosphere 5*, 651–657.

Crowley, T. J. & Hyde, W. T. 2008: Transient nature of Late Pleistocene climate variability. *Nature 456*, 226–230.

Csató, I., Tóth, S., Catuneau, O. & Granjeon, D. 2015: A sequence stratigraphic model for the Upper Miocene–Pliocene basin fill of the Pannonian Basin, eastern Hungary. *Marine and Petroleum Geology 66*, 117–134.

De Schepper, S., Gibbard, P. L., Salzmann, U. & Ehlers, J. 2014: A global synthesis of the marine and terrestrial evidence for glaciation during the Pliocene Epoch. *Earth-Science Reviews 135*, 83–102.

Dearing, J. A., Dann, R. J. L., Hay, K., Lees, J. A., Loveland, P. J., Maher, B. A. & O'Grady, K. 1996: Frequency-dependent susceptibility measurements of environmental materials. *Geophysical Journal International 104*, 228–240.

Deng, C. L., Zhu, R. X., Verosub, K. L., Singer, M. J., Liu, Q. S., Shaw, J. & Zhu, R. X. 2004: Mineral magnetic properties of loess/paleosol couplets of the central loess plateau of China over the last 1.2 Myr. *Journal of Geophysical Research 109*, B01103, https://doi.org/10.1029/2003JB002532.

Dunlop, D. J. & Özdemir, Ö. 1997: *Rock Magnetism: Fundamentals and Frontiers.* 573 pp. Cambridge University Press, New York.

Ehlers, J. & Gibbard, P. L. 2007: Glaciations – overview. *In* Elias, S. A. (ed.): *Encyclopedia of Quaternary Science*, 1023–1031. Elsevier, Amsterdam.

Ehlers, J., Gibbard, P. L. & Hughes, P. D. 2011: *Quaternary Glaciations – Extent and Chronology. A Closer Look*. 1126 pp. Elsevier, Amsterdam, Edinburgh, Oxford.

Elston, D. P., Lantos, M. & Hámor, T. 1994: High resolution polarity records and the stratigraphic and magnetostratigraphic correlation of Late Miocene and Pliocene (Pannonian s.l.) deposits of Hungary. *In* Teleki, P. G., Mattick, R. E. & Kókai, J. (eds.): *Basin Analysis in Petroleum Exploration. A Case Study from the Békés Basin, Hungary*, 111–142. Kluwer Academic Publishers, Dordrecht.

Fischer, H., Luster, J. & Gehring, A. U. 2007: Magnetite weathering in a vertisol with seasonal redox-dynamics. *Geoderma 143*, 41–48.

Foufoula-Georgiou, E. & Kumar, P. (eds.) 1994: *Wavelets in Geophysics.* 384 pp. Academic Press, San Diego.

Grimley, D. A. & Arruda, N. K. 2007: Observations of magnetite dissolution in poorly drained soils. *Soil Science Society of America Journal 172*, 968–982.

Gruber, S. & Haeberly, W. 2007: Permafrost in steep bedrock slopes and its temperature-related destabilization following climate change. *Journal of Geophysical Research 112*, F02S18, https://doi.org/10.1029/2006JF000547.

Gruber, S. & Haeberly, W. 2009: Mountain permafrost. *In* Margesin, R. (ed.): *Permafrost Soils, Soil Biology*, vol. *16*, 33–44. Springer-Verlag, Berlin.

Hansen, J., Sato, M., Kharecha, P., Beerling, B., Berner, R., Masson-Delmotte, V., Pagani, M., Raymo, M. E., Royer, D. L. & Zachos, J. C. 2008: Target atmospheric CO_2: where should humanity aim? *Open Atmospheric Sciences 2*, 217–223.

Hays, J. D., Imbrie, I. & Shackleton, N. J. 1976: Variations in the Earth's orbit: pacemaker of the ice ages. *Science 194*, 1121–1132.

Head, M. J. & Gibbard, P. L. 2005: Early–Middle Pleistocene transitions: an overview and recommendation for the defining boundary. *Geological Society, London, Special Publications 247*, 1–18.

Heider, F., Bock, J. M., Hendy, I., Kennett, J. P., Matzka, J. & Schneider, J. 2001: Latest Quaternary rock magnetic record of climatic and oceanic change, Tanner Basin, California borderland. *Geological Society of America Bulletin 113*, 346–359.

Hilgen, F. J. 1991: Extension of the astronomically calibrated (polarity) time scale to the Miocene/Pliocene boundary. *Earth and Planetary Science Letters 107*, 349–368.

Hughes, P. D. & Gibbard, P. L. 2014: A stratigraphical basis for the Last Glacial Maximum (LGM). *Quaternary International 383*, 174–185.

Imbrie, J. & Imbrie, K. P. 1979: *Ice Ages. Solving the Mystery*. 244 pp. Harvard University Press, Cambridge.

Imbrie, J. & Imbrie, J. Z. 1980: Modelling the climate response to orbital variations. *Science 207*, 943–953.

Jansen, E., Sjøholm, J., Bleil, U. & Erichsen, J. A. 2017: Ice rafted debris of ODP Hole 104-642B. PANGAEA, https://doi.org/10.1594/PANGAEA.882966 in supplement to Jansen, E., Sjøholm, J., Bleil, U. & Erichen, J. A. 1990: Neogene and Pleistocene glaciations in the northern hemisphere and late Miocene–Pliocene global ice volume fluctuations: Evidence from the Norwegian Sea. *In* Bleil, U. & Thiede, J. (eds.): *Geological History of the Polar Oceans: Arctic Versus Antarctic*, 677–705. Kluwer Academic Publishers, Dordrecht.

Johnsen, S. J., Dahl-Jensen, D., Gundestrup, N., Steffensen, J. P., Clausen, H. B., Miller, H., Masson-Delmotte, V., Sveinbjornsdottir, A. E. & White, J. 2001: Oxygen isotope and palaeotemperature records from six Greenland ice-core stations: Camp Century, Dye-3, GRIP, GISP2, Renland, and NorthGRIP. *Journal of Quaternary Science 16*, 299–307.

Jouzel, J. & Masson-Delmotte, V. 2010: Deep ice cores: the need for going back in time. *Quaternary Science Reviews 29*, 3683–3689.

Jouzel, J. and 31 others 2007: Orbital and millennial Antarctic climate variability over the past 800,000 years. *Science 317*, 793–796.

Juhász, G., Pogácsás, G., Magyar, I. & Vakarcs, G. 2007: Tectonic versus climatic control on the evolution of fluvio-deltaic systems in a lake basin, Eastern Pannonian Basin. *Sedimentary Geology 202*, 72–95.

Kawase, H., Yamazaki, T., Sugimoto, S., Sasai, T., Ito, R., Hamada, T., Kuribayashi, M., Fujita, M., Murata, A., Nosaka, M. & Sasaki, H. 2020: Changes in extremely heavy and light snow-cover winters due to global warming over high mountainous areas in central Japan. *Progress in Earth and Planetary Science 7*, 10, https://doi.org/10.1186/s40645-020-0322-x.

Kelder, N. A., Sant, K., Dekkers, M. J., Magyar, I., van Dijk, G. A., Lathouwers, Y. Z., Sztanó, O. & Krijgsman, W. 2018: Paleomagnetism in Lake Pannon: problems, pitfalls, and progress in using iron sulfides for magnetostratigraphy. *Geochemistry, Geophysics, Geosystems 19*, 3405–3429.

Kent, D. V. 1999: Orbital tuning of geomagnetic polarity time-scales. *Philosophical Transactions of the Royal Society of London 357*, 1995–2007.

Koson, S., ChernaiI, P. & Choowong, M. 2014: Seismic attributes and their applications in seismic geomorphology. *Bulletin of Earth Sciences of Thailand 6*, 1–9.

Krolopp, E. 1977: *Pleistocene Mollusc Fauna from Borehole Dévaványa-1*. 15 pp. Geological and Geophysical Institute of Hungary, Budapest.

Laskar, J. 1989: A numerical experiment on the chaotic behaviour of the solar system. *Nature 338*, 237–238.

Laskar, J., Fienga, A., Gastineau, M. & Manche, H. 2011: La2010: a new orbital solution for the long-term motion of the Earth. *Astronomy & Astrophysics 532*, A89, https://doi.org/10.1051/0004-6361/201116836.

Laskar, J., Joutel, F. & Boudin, F. 1993: Orbital, precessional, and insolation quantities for the Earth from −20 Myr to +10 Myr. *Astronomy and Astrophysics 270*, 522–533.

Laskar, J., Robutel, P., Joutel, F., Gastineau, M., Correia, A. C. M. & Levrard, B. 2004: A long-term numerical solution for the insolation quantities of the Earth. *Astronomy and Astrophysics 428*, 261–285.

Lehner, B. & Grill, G. 2013: Global river hydrography and network routing: baseline data and new approaches to study the world's large river systems. *Hydrological Processes 27*, 2171–2186.

Lenaerts, J. T. M., Vizcanio, M., Fyke, J., van Kampenhout, L. & van den Broeke, M. C. 2016: Present-day and future Antarctic ice sheet climate and surface mass balance in the Community Earth System Model. *Climate Dynamics 47*, 1367–1381.

Leonhardt, R. 2006: Analyzing rock magnetic measurements: The Rock-MagAnalyzer 1.0 software. *Computers and Geosciences 32*, 1420–1431.

Lewin, J. & Ashworth, P. J. 2014: Defining large river channel patterns: alluvial exchange and plurality. *Geomorphology 215*, 83–98.

Lisiecki, L. E. & Raymo, M. E. 2005: A Plio-Pleistocene stack of 57 globally distributed benthic $\delta^{18}O$ records. *Paleoceanography and Paleoclimatology 20*, PA1003, https://doi.org/10.1029/2004PA001071.

Magyar, I. 2015: Palaeobiogeography of lacustrine cockles as a tool to reconstruct palaeogeography in the Late Neogene Paratethys. *Hantkeniana 10*, 143–146.

Magyar, I. 2021: Chronostratigraphy of clinothem-filled non-marine basins: dating the Pannonian stage. *Global and Planetary Change 205*, 103609, https://doi.org/10.1016/j.goplacha.2021.103609.

Magyar, I. & Sztanó, O. 2008: Is there a Messinian unconformity in the Central Paratethys? *Stratigraphy 5*, 245–255.

Magyar, I., Radivojević, D., Sztanó, O., Synak, R., Ujszászi, K. & Pócsik, M. 2013: Progradation of the paleo-Danube shelf margin across the Pannonian Basin during the Late Miocene and Early Pliocene. *Global and Planetary Change 103*, 168–173.

Mahrez, H. B., Márton, P., Márton, B., Mádl-Szőnyi, J., Kovács, J. & Sztanó, O. 2023: Hydrostratigraphic decomposition of fluvio-deltaic sediments inferred from seismic morphology and geophysical well logs in the Pannonian Basin, Hungary. *Global and Planetary Change 230*, 104285, https://doi.org/10.1016/j.géoplacha.2023.104285.

Marty, C. 2013: Climate change and snow cover in the European Alps. *In* Rixen, C. & Rolando, A. (eds.): *The Impacts of Skiing on Mountain Environments*, 30–44. Bentham Science Publishers, Sharjah.

Miall, A. D. 1996: *The Geology of Fluvial Deposits*. 582 pp. Springer, Berlin, Heidelberg, New York.

Milankovitch, M. 1941: *Kanon der Erdbestrahlung und seine Andwendung auf das Eiszeitenproblem*. 633 pp. Royal Serbian Academy, Belgrade.

Minár, J., Bizubová, M. & Gallay, M. 2004: General aspects of denudation chronology of the West Carpathians. *Studia Geomorphologica Carpatho-Balcanica 38*, 5–22.

Nádor, A., Lantos, M., Tóth-Makk, Á. & Thamó-Bozsó, E. 2003: Milankovich-scale multy-proxy records from fluvial sediments of the last 2.6 Ma, Pannonian basin, Hungary. *Quaternary Science Reviews 22*, 2157–2175.

Nederbragt, A. J., Francus, P., Bollmann, J. & Soreghan, M. J. 2005: Image calibration, filtering, and processing. *In* Francus, P. (ed.): *Image Analysis, Sediments and Paleoenvironments*, 35–58. Kluwer Academic Publishers, Dordrecht.

Nelson, E., Püspöki, Z., McIntosh, R. W., Presslee, S., Szappanos, B., White, D. & Penkman, K. 2023: Constraining the chronology of Quaternary fluvial sediments in the Pannonian Basin. *XXI INQUA Congress 2023, poster session on Marine and terrestrial records: new perspectives for Quaternary climatic changes.*

Obu, J., Westermann, S., Bartsch, A., Berdnikov, N., Christiansen, H. H., Dashtseren, A., Delaloye, R., Elberling, B., Etzelmüller, B., Kholodov, A., Khomutov, A., Kaab, A., Leibman, M. O.,

Lewkowicz, A. G., Panda, S. K., Romanovsky, V., Way, R. G., Westergaard-Nielsen, A., Wu, T., Yamkhin, J. & Zou, D. 2019: Northern Hemisphere permafrost map based on TTOP modelling for 2000–2016 at 1 km^2 scale. *Earth-Science Reviews 193*, 299–316.

Paillard, D. L., Labeyrie, M. A. & Yiou, P. 1996: Macintosh program performs time-series analysis. *Eos, Transactions American Geophysical Union 77*, 379.

Paterson, G. A., Zhao, X., Jackson, M. & Heslop, D. 2018: Measuring, processing, and analyzing hysteresis data. *Geochemistry, Geophysics, Geosystems 19*, 1925–1945.

Petit, J. R., Jouzel, J., Raynaud, D., Barkov, N. I., Barnola, J.-M., Basile, I., Bender, M., Chappellaz, J., Davis, M., Delaygue, G., Delmotte, M., Kotlyakov, V. M., Legrand, M., Lipenkov, V. Y., Lorius, C., Pépin, L., Ritz, C., Saltzman, E. & Stievenard, M. 1999: Climate and atmospheric history of the past 420,000 years from the Vostok ice core, Antarctica. *Nature 399*, 429–436.

Pogácsás, G., Mattick, R. E., Elston, D. P., Hámor, T., Jámbor, Á., Lakatos, L., Lantos, M., Simon, E., Vakarcs, G., Várkonyi, L. & Várnai, P. 1994: Correlation of seismo- and magnetostratigraphy in southeastern Hungary. *In* Teleki, P. G., Mattick, R. E. & Kókay, J. (eds.): *Basin Analysis in Petroleum Exploration. A Case Study from the Békés Basin, Hungary*, 143–160. Kluwer Academic Publishers, Dordrecht.

Popescu, R., Onaca, A., Urdea, P. & Vespremeanu-Stroe, A. 2017: Spatial distribution and main characteristics of alpine permafrost from southern Carpathians, Romania. *In* Radoane, M. & Vespremeanu-Stroe, A. (eds.): *Landform Dynamics and Evolution in Romania*, 117–146. Springer Geography, Springer, Cham.

Püspöki, Z., Fogarassy-Pummer, T., Thamó-Bozsó, E., Berényi, B., Cserkész-Nagy, Á., Szappanos, B., Márton, E., Lantos, Z., Nádor, A., Fancsik, T., Stercel, F., Tóth-Makk, Á., McIntosh, R. W., Szőcs, T. & Faragó, E. 2020: High-resolution stratigraphy of a Quaternary fluvial deposit based on magnetic susceptibility variations (Jászság Basin, Hungary). *Boreas 49*, 181–199.

Püspöki, Z., Fogarassy-Pummer, T., Thamó-Bozsó, E., Falus, G., Cserkész-Nagy, Á., Szappanos, B., Márton, E., Lantos, Z., Szilárd, S., Stercel, F., Tóth-Makk, Á., McIntosh, R. W., Szőcs, T., Pálóczy, P. & Fancsik, T. 2021a: High-resolution stratigraphy of Quaternary fluvial deposits in the Makó Trough and the Danube-Tisza Interfluve based on magnetic susceptibility data (Pannonian Basin, Hungary). *Boreas 50*, 205–223.

Püspöki, Z., Gibbard, P. L., Kiss, L. F., McIntosh, R. W., Thamó-Bozsó, E., Krassay, Z., Szappanos, B., Maigut, V., Kovács, P., Karácsony, D., Stercel, F., Visnovitz, F., Demény, K., Bereczki, L., Szőcs, T., Rotár-Szalkai, Á. & Fancsik, T. 2023: Obliquity-driven mountain permafrost-related fluvial magnetic susceptibility cycles in the Quaternary mid-latitude long-term (2.5 Ma) fluvial Maros Fan in the Pannonian Basin. *Boreas 52*, 402–426.

Püspöki, Z., Gibbard, P. L., Nádor, A., Thamó-Bozsó, E., Sümegi, P., Fogarassy-Pummer, T., McIntosh, R. W., Lantos, M., Tóth-Makk, Á., Stercel, F., Krassay, Z., Kovács, P., Szőcs, T. & Fancsik, T. 2021b: Fluvial magnetic susceptibility as a proxy on long-term variations of mountain permafrost development in the Alp-Carpathian Region. *Boreas 50*, 806–825.

Püspöki, Z., Kovács, I. J., Fancsik, T., Nádor, A., Thamó-Bozsó, E., Tóth-Makk, Á., Udvardi, B., Konya, P., Füri, J., Bendő, Z., Zilahi-Sebess, L., Stercel, F., Gulyás, Á. & McIntosh, R. W. 2016: Magnetic susceptibility as a possible correlation tool in Quaternary alluvial stratigraphy. *Boreas 45*, 861–875.

Randazzo, N. A., Michalak, A. M., Miller, C. E., Miller, S. M., Shiga, Y. P. & Fang, Y. 2021: Higher autumn temperatures Lead to contrasting CO_2 flux responses in boreal forests versus tundra and Shrubland. *Geophysical Research Letters 48*, 93843, https://doi.org/10.1029/2021GL093843.

Raymo, M. E., Lisiecki, L. E. & Nisancioglu, K. 2006: Plio–Pleistocene ice volume, Antarctic climate and the global $\delta^{18}O$ record. *Science 313*, 492–495.

Raymo, M. E., Ruddiman, W. F., Backman, J., Clement, B. M. & Martinson, D. G. 1989: Late Pliocene variations in northern hemisphere ice sheets and North Atlantic deep-water circulation. *Paleoceanography 4*, 413–446.

Royden, L. H. & Horváth, F. (eds.) 1988: The Pannonian Basin: a study in basin evolution. *AAPG Memoir 45*, 1–394.

Ruddiman, W. F. & McIntyre, A. 1984: Ice-age thermal response and climatic role of the surface Atlantic Ocean, 40°N to 63°N. *Geological Society of America Bulletin 95*, 381–396.

Ruddiman, W. F., Raymo, M. & McIntyre, A. 1986: Matuyama 41,000-year cycles, North Atlantic Ocean and northern hemisphere ice sheets. *Earth and Planetary Science Letters 80*, 117–129.

Schroeder, P. A., Le Golvan, J. J. & Roden, M. F. 2002: Weathering of ilmenite from granite and chlorite schist in the Georgia Piedmont. *American Mineralogist 87*, 1616–1625.

Seki, O., Foster, G. L., Schmidt, D. N., Mackensen, A., Kawamura, K. & Pancost, R. D. 2010: Alkenone and boron-based Pliocene pCO_2 records. *Earth and Planetary Science Letters 292*, 201–211.

Shackleton, N. 1967: Oxygen isotope analyses and Pleistocene temperatures re-assessed. *Nature 215*, 15–17.

Sütő-Szentai, M. 2022: Database of organic-walled microplankton zones in Hungary (Upper Miocene, Pliocene). *E-Acta Naturalia Pannonica 23*, 5–88.

Sztanó, O., Szafián, P., Magyar, I., Horányi, A., Bada, G., Hughes, D. W., Hoyer, D. L. & Wallis, R. J. 2013: Aggradation and progradation controlled clinothems and deep-water sand delivery model in the Neogene Lake Pannon, Makó Trough, Pannonian Basin, SE Hungary. *Global and Planetary Change 103*, 149–167.

Thomson, D. J. 1982: Spectrum estimation and harmonic analysis. *Proceedings of the IEEE 70*, 1055–1096.

Thomson, D. J. 1990: Quadratic-inverse spectrum estimates; applications to paleoclimatology. *Philosophical Transactions: Physical Sciences and Engineering 332*, 539–597.

Tiedemann, R., Sarnthein, M. & Shackleton, N. J. 1994: Astronomic timescale for the Pliocene Atlantic $\delta^{18}O$ and dust flux records of Ocean Drilling Program site 659. *Paleoceanography 9*, 619–638.

Torrence, C. & Compo, G. P. 1998: A practical guide to wavelet analysis. *Bulletin of the American Meteorological Society 79*, 61–78.

Uhrin, A. & Sztanó, O. 2023: Zagyvai Formáció. *In* Babinszki, E., Piros, O., Csillag, G., Fodor, L., Gyalog, L., Kercsmár, Z., Less, G., Lukács, R., Sebe, K., Selmeczi, I., Szepesi, J. & Sztanó, O. (eds.): *Magyarország litosztratirájfiai egységeinek leírása II. Kainozóos képződmények*, p. 132. Szabályozott Tevékenységek Felügyeleti Hatósága, Budapest.

Wapenhans, I., van der Beek, P., Bernard, M., Colleps, C. & Amalberti, J. 2024: Reconciling late Cenozoic spatio-temporal patterns of Alpine topographic changes from low-temperature thermochronology and glacial morphometric signatures. EGU General Assembly 2024, Vienna, Austria, 14–19 April 2024, EGU24-16703, https://doi.org/10.5194/egusphere-egu24-16703.

Weedon, G. P. 2003: *Time-Series Analysis and Cyclostratigraphy – Examining Stratigraphic Records of Environmental Cycles*. 259 pp. Cambridge University Press, Cambridge.

Zan, J., Fang, X., Yang, S., Nie, J. & Li, X. 2010: A rock magnetic study of loess from the West Kunlun Mountains. *Journal of Geophysical Research 115*, B10101, https://doi.org/10.1029/2009JB007184.

Supporting Information

Additional Supporting Information to this article is available at http://www.boreas.dk.

Data S1. Calculation of the superparamagnetic content of sample 896.00 m.

Fig. S1. Facies interpretation of the Zagyva Formation based on sediment log interpretation of the Dévaványa borehole and time slices of the 3D seismic block enclosing the long core. For the vertical position of the focused log intervals see Fig. 3, for the position of the seismic time slices see Fig. 2B.

Fig. S2. Strike-orientated vertical section (up) and its stratigraphical interpretation (down) close to the Dévaványa section, presenting positive flower structures reaching the Quaternary succession, but not touching the cored site.

Fig. S3. Work procedure of correlation of monthly insolation averages at 47°N and Dévaványa χ_{LF} record. Top: The generation of insolation curves (monthly averages) (Laskar *et al*. 2004) in AnalySeries (Paillard *et al*. 1996) between −2000 and 8000 ka, to avoid marginal distortion during the filtering. The months were defined from 6th day to 5th day to ensure symmetry around the Vernal Point (thus starting with −15–15 degree for March). Middle: The resampled envelopes of filtered curves. The filtering (Gaussian filter, fw = 0.01, bw = 0.002 1 ka^{-1}) and Hilbert transformation (AM filter in AnalySeries) were performed on the −2000–8000 ka time series and the result was resampled to the 0–5300 interval. Bottom: Cross-correlation of the resampled envelopes with the envelope of the filtered χ_{LF} record (Fig. 7) and calculation of the correlation coefficient (R) as the absolute value of the minimum at or very close to the X(lag time) = 0. The procedure was repeated cyclically performing the monthly insolation curves for 37°N, 57°N, 65°N. For R values see Fig. 8.

Fig. S4. Insolation curves (monthly averages) in the polar regions (Laskar *et al*. 2004) generated in AnalySeries (Paillard *et al*. 1996) between −2000 and 8000 ka. Top: 78°S (the latitude of the Vostok Station in Antarctica). Bottom: 72°S (the latitude of Summit Station in Greenland).